The response to ketogenic diet in colorectal cancer is mediated by lasting functional alterations of the gut microbiome

Mina Tsenkova[1], Madita Brauer[1,2], Marat Kasakin[3], Susheel Bhanu Busi[3,4], Maryse Schmoetten[1], Anthoula Gaigneaux[5], Vitaly Pozdeev[1], Marianne Meyers[1], Eric Koncina[1], Diran Herebian[6], Fabien Rodriguez[1], Martine Schmitz[1], Laura de Nies[3], Ertan Mayatepek[6], Serge Haan[1], Carine de Beaufort[7], Jérôme Graas[8], Thorsten Cramer[9], Carole Linster[3], Paul Wilmes[3,5], Elisabeth Letellier[1]

[1] Molecular Disease Mechanisms Group, Department of Life Sciences and Medicine, Faculty of Science, Technology and Medicine, University of Luxembourg, Esch-sur-Alzette, Luxembourg

[2] Institute for Advanced Studies, University of Luxembourg, Esch-sur-Alzette, Luxembourg

[3] Luxembourg Centre for Systems Biomedicine, University of Luxembourg, Esch-sur-Alzette, Luxembourg

[4] UK Centre for Ecology and Hydrology, Wallingford, United Kingdom

[5] Department of Life Sciences and Medicine, Faculty of Science, Technology and Medicine, University of Luxembourg, Esch-sur-Alzette, Luxembourg

[6] Department of General Pediatrics, Neonatology and Pediatric Cardiology, Medical Faculty and University Hospital Düsseldorf, Heinrich Heine University, Düsseldorf, Germany

[7] Pediatric Clinic, Centre Hospitalier de Luxembourg, Luxembourg, Luxembourg

[8] Centre d'Investigation et d'Epidémiologie Clinique, Luxembourg Institute of Health, Hesperange, Luxembourg

[9] Molecular Tumor Biology, Department of General, Visceral and Transplantation Surgery, RWTH University Hospital Aachen, Germany

Abstract

Colorectal cancer (CRC) patients have been shown to possess an altered gut microbiome. Diet is a known microbiome modulator. An attenuating effect of the ketogenic diet (KD) on CRC cell growth has been previously observed, however the role of the gut microbiome in driving this effect remains unknown. Here, we describe a reduced colonic tumor burden upon KD consumption in a CRC mouse model with a humanized microbiome. Importantly, we demonstrate a causal relationship through microbiome transplantation into germ-free mice, whereby alterations in gut microbial function were maintained in the absence of continued selective pressure from the KD. Stearic acid is identified as a putative microbiome-derived anti-cancer metabolite. Taken together, the beneficial effects of the KD are mediated by the gut microbiome and may be dependent on a pre-existing “non-responder” or “responder” gut microbiome profile. These results have important implications for future clinical trials evaluating the effects of the ketogenic diet on human CRC.

43 **Introduction**

44 Worldwide, colorectal cancer (CRC) is the third most prevalent cancer, with over 1.9 million new
45 cases recorded in 2020[1]. CRC incidence and mortality rates have been associated with various lifestyle-
46 related risk factors, in particular dietary habits. Recent years have seen a rise in CRC incidence in persons
47 aged 50 years and under, further underlining the importance of studying these factors[2]. The ketogenic
48 diet (KD) has been shown to possess anti-cancer properties in the context of CRC, and many studies have
49 focused on the importance of the restriction of energy to slow the growth of rapidly proliferating cells and
50 anti-cancer signaling through ketone bodies[3]. One recently published study investigated the effects of the
51 KD on CRC development and described a new mechanism through which KD exerts its anti-cancer effects,
52 namely through the ketone body β-hydroxybutyrate acting on the surface receptor Hcar2, inducing the
53 transcriptional regulator *Hopx*, thus altering gene expression and inhibiting cell proliferation[4]. These
54 studies often focus on the effects of KD on the cancer cells themselves, and rarely on other cells of the
55 tumor microenvironment (TME), such as immune cells[5,6] and cancer-associated fibroblasts (CAFs)[7], or on
56 external factors, such as the gut microbiome. Specifically in CRC, cancer progression is accompanied by a
57 state of dysbiosis of the gut microbiome[8]. The study of the role of the different bacteria in CRC is of
58 particular interest, considering the affected tissue type is in contact with the gut microbiome. Until
59 recently, few studies had investigated the effects of the KD on the gut microbiome in health and disease[9],
60 but this has now changed, with a number of new studies published over the last three years[6,8]. These
61 studies remain largely descriptive regarding dietary-induced gut microbiome changes and the role of the
62 gut microbiome in maintaining the reported anti-cancer effects of the KD in the context of CRC has not
63 yet been investigated.

64

65

66

67 **Results**

68 **KD leads to reduced colonic tumor burden and inflammatory response in CRC**

69 To study the relevance of the gut microbiome in CRC development in a model relevant to human
70 disease, we first established a representative healthy human microbiome by mixing fecal samples from
71 five healthy donors (5HD; Extended Data Fig. 1a for patient metadata). The achieved 5HD mix
72 recapitulated the compositions of the individual donor samples, as evidenced by family, genus and species
73 level analysis of whole genome shotgun sequencing (WGS, Extended Data Fig. 1b-d, respectively), while
74 fecal metabolite levels varied across samples (Extended Data Fig. 1e). We performed fecal microbial
75 transplantation (FMT) of the 5HD mix into germ-free (GF) and antibiotic-treated specific-pathogen-free
76 (SPF) mice in an AOM/DSS CRC model (Fig. 1a and 1b, details can be found in the methods section)
77 followed by a switch from standard to ketogenic diet after the last cycle of DSS. No significant difference
78 in body weight between the standard diet (SD) and ketogenic diet (KD) groups was observed throughout
79 the experiments, although dips in mouse body weight were observed following the antibiotic treatment
80 and following each cycle of DSS (Extended Data Fig. 2a and 2b). There was no difference in colon length
81 between groups (Extended Data Fig. 2c, GF). KD-fed mice exhibited a lower colonic tumor burden (Fig. 1c
82 (GF) and Fig. 1d (SPF)) and a smaller tumor size (Fig. 1e, 1f and 1g (SPF)) than SD-fed mice.

83 Characterization of full-length lamina propria (LP), mesenteric lymph node (MLN) and spleen
84 immune cell profiles (Extended Data Fig. 2d and 2e) showed a reduction in almost all LP $CD4^+$ T cell
85 populations in KD-fed mice. Only LP natural killer T cells and type 3 innate lymphoid cells (GF LP) were
86 increased – both have been associated to gut homeostasis and health[10]. Finally, the expression of both
87 subunits of calprotectin (a biomarker of inflammation used in inflammatory bowel disease[11]) was reduced
88 in the spleens of GF KD-fed mice (Extended Data Fig. 2f and 2g). Nevertheless, it remains unclear whether
89 the reduction in immune cell populations reflects reduced inflammation induced by the KD or is rather a
90 direct consequence of the reduced tumor development.

91 To further assess the importance of KD in modulating inflammation in CRC, we employed a low-
92 grade inflammatory model, in which mice received four doses of AOM and were randomized into one of
93 three subgroups - GF, 5HD mix FMT, single CRC patient FMT, each with a KD and SD branch (Extended
94 Data Fig. 3a, 3b (5HD) and 3c (CRC)). A single CRC donor was used for colonization, rather than a mix of
95 multiple samples, due to the observed dissimilarities of microbial profiles between patients in our in-
96 house CRC stool collection. Despite the induction of ketosis in KD-fed mice (Extended Data Fig. 3d), we
97 observed no significant differences in colonic tumor burden between groups (Extended Data Fig. 3e), nor
98 in immune cell profiles (Extended Data Fig. 3f), suggesting not only that the KD specifically exerted its anti-
99 cancer effect in an inflammatory setting, independent of ketosis, likely by reducing inflammation, but also
100 that the fecal microbiome from this CRC patient did not exhibit a higher potential for CRC induction in this
101 setting, in contrast to observations made by Wong et al.[12]. Of note, long-term KD feeding induced fatty
102 liver and fibrosis in all sub-groups (Extended Data Fig. 3g), and as previously reported for long-term KD
103 consumption[13]. Altogether, these results suggest that the KD exerts an anti-tumorigenic effect in CRC,
104 potentially by modulating the immune system.
105
106 **KD induces a distinct host metabolic profile**
107 Ordination analyses based on the underlying β-diversity among host plasma samples collected
108 from animals undergoing ketogenic dietary intervention in the AOM/DSS inflammatory model of CRC,
109 revealed clustering based on dietary condition (Extended Data Fig. 4a (SPF) an Extended Data Fig. 4b (GF)).
110 β-HB plasma levels were elevated in KD-fed mice (Extended Data Fig. 4c (SPF) and 4d (GF)), confirming
111 ketosis. KD-fed mice presented altered amino acid, fatty acid, sugar, carbohydrate, vitamin, and bile acid
112 metabolism (Supp. Table 1 and Extended Data Fig. 4e (SPF), Supp. table 2 and Supp Fig. 4f (GF).
113 Furthermore, mannose was increased in KD-fed mice (Supp. Table 1 (SPF) and 2(GF)). Interestingly,
114 mannose has been reported to possess antitumor properties[14], impairing tumor cell growth *in vitro* and

115 *in vivo*[15], and targeting tumor-associated macrophages[16]. While treatment with β-hydroxybutyrate
116 showed no effect, treatment with the ketone bodies acetone and sodium acetoacetate tended to reduce
117 the differentiation of naive T cells into Th17 cells (Extended Data Fig. 4g and 4h), which play an important
118 role in maintaining gut homeostasis[17] and are affected by KD in a dose-dependent manner[5]. Treatment
119 with a commercially available lipid mixture mimicking KD (containing arachidonic, linoleic, linolenic,
120 myristic, oleic, palmitic and stearic acid) led to a dose-dependent reduction in Th17 differentiation
121 (Extended Data Fig. 4i), as did treatment with some individual fatty acids, such as palmitic and oleic acid
122 (Extended Data Fig. 4j), suggesting that Th17 cells are susceptible to fatty acid modulation, but that
123 different fatty acids may exhibit different effects. Collectively, these data indicate that KD induces
124 systemic functional metabolic changes in the host, which are not limited to the induction of ketosis.
125
126 **The anti-cancer effects of the KD are mediated by the gut microbiome**
127 The gut microbiome may affect CRC development either by directly interacting with host cells
128 (attachment, invasion and translocation), or indirectly, through bacterial metabolism (genotoxins, SCFAs
129 and others)[18]. We first excluded bacterial translocation as a primary factor in the KD-mediated phenotype,
130 as mucus layer thickness (Extended Data Fig. 5a and 5b (GF)) and LPS levels in plasma (Extended Data Fig.
131 5c (GF) and 5d (SPF)) remained unaltered upon KD consumption, in line with Ang et al.[5]. To test the causal
132 role of the gut microbiome in our experimental setup, we performed a similar experiment in humanized
133 gut microbiome GF mice, however we housed the mice in open-top cages in a gnotobiotic flexible-film
134 isolator to allow for microbial exchange between groups (Extended Data Fig. 5e, 5f and 5g). Despite
135 confirmed ketosis, no difference in colonic tumor burden (Extended Data Fig. 5h), nor in colonic tumor
136 size (Extended Data Fig. 5i and 5j) was observed between groups. Furthermore, fecal microbial
137 compositions were similar in both groups (Extended Data Fig. 5k), with only a few taxa differentially
138 abundant between groups (Extended Data Fig. 5l), suggesting that microbial exchange between mice on

139 KD and SD was sufficient to negate the beneficial effects of the KD. Most importantly, we next performed
140 cecal microbial transplantation (CMT) of samples collected from the SPF diet mice (Fig. 1d) into a next
141 generation of SD-fed GF mice undergoing the same cancer model (Fig. 2a, Extended Data Fig. 5m).
142 Strikingly, KD-CMT mice, exhibited a lower colonic tumor burden than SD-CMT mice (Fig. 2b). Average
143 colonic tumor size per mouse did not differ between groups (Fig. 2c), however, KD-CMT mice exhibited a
144 smaller proportion of large tumors (Fig. 2d and e). Altogether, our results demonstrate the causal role of
145 the gut microbiome in mediating the previously observed KD-driven anticancer effect.
146
147 **KD induces a distinct fecal microbial profile**
148 Ordination analyses based on the underlying β-diversity among fecal samples collected from KD-
149 and SD-fed AOM/DSS mice revealed clustering of 5HD mix used for FMT with the individual healthy donor
150 stool samples and with the murine stool samples collected three days after FMT (TG, Extended Data Fig.
151 6a (SPF) and Extended Data Fig. 6d (GF)), confirming the validity of the 5HD mix used for transplant and
152 its engraftment. Furthermore, we observed increasing differences between KD and SD samples over time
153 (Extended Data Fig. 6b (SPF) and Extended Data Fig. 6e (GF)). Early time points cluster together (T0,
154 collected at diet change), while later time points diverge (T1-T4). Differential analysis revealed
155 *Akkermansia* spp., bacteria which can suppress colorectal tumorigenesis through modulation of the
156 immune system[19], *Intestimonas* spp., *Lachnoclostridium* spp., *Bilophila* spp. (Extended Data Fig. 6c (SPF)),
157 *Phocea* spp., *Faecalitalea* spp. and others (Extended Data Fig. 6f (GF), Supp. Table 3 (SPF) and 4 (GF)) to
158 be more abundant in KD, while *Bifidobacterium* spp., *Turicibacter* spp. (SPF), *Barnesiella* spp.,
159 *Eisenbergiella* spp., *Ruminococcus 1* and *2* spp. (GF) and others were depleted. Furthermore, the
160 differential abundance of various members of *Barnesiellaceae* spp., *Erysipelotrichaceae* spp.,
161 *Lachnospiraceae* spp. and *Ruminococcaceae* spp. suggested that dietary composition affects bacterial
162 members of the same families in different manners.

163 Investigation of the engrafted gut microbial communities at experimental endpoint revealed
164 distinct KD- and SD-associated microbiomes (Fig. 3a and 3b, Extended Data Fig. 6g, 6h (GF), 6i and 6j), as
165 well as KD-CMT- and SD-CMT-associated microbiomes (Fig. 3a and 3b, Extended Data Fig. 6i and 6j).
166 Although a selective pressure of the KD was observed, gut microbial composition differed between cecal
167 donor and recipient mice, likely due to the absence of continued selective pressure from the KD, or loss
168 of more fragile and hard-to-engraft bacteria (Fig. 3a). Metagenome-assembled genomes (MAGs),
169 representing abundant members of the microbial community, allowed us to achieve species-level
170 resolution. Noteworthy, some MAGs annotated as CRC-associated bacteria, such as *Rikenellaceae* spp.
171 (light blue) and *Muribaculaceae* spp. (dark blue, Fig. 3c, Extended Data Fig. 6k (GF)), were detected in SD
172 groups but not the KD groups. Interestingly, various *Alistipes* spp. were differentially abundant in all
173 experiments. Two MAGs (*Alistipes* and *COE* species) were only identified in KD-CMT, while 12 MAGs were
174 only identified in SD-CMT, among which *CAG-873*, *CAG-48* and *Parabacteroides distasonis* (Fig. 3c), also
175 identified in the donor SPF dietary experiment.
176
177 **Distinct fecal microbial functional profiles are maintained upon FMT**
178 Furthermore, as microbiome-mediated effects are based on the functional and metabolic
179 capacities of different microbes, we also investigated KD-induced functional changes. β-diversity analysis
180 based on KEGG and Pfam ordinations of SPF fecal samples revealed a clear separation between groups
181 (Extended Data Fig. 7a (KEGG) and 7b (Pfam)), suggesting selective pressure of the diet on the intestinal
182 microbiota. This could also be observed in the CMT experiment, where KD-CMT clustered separately from
183 SD-CMT, despite being maintained on SD (Extended Data Fig. 7c (KEGG) and 7d (Pfam)). Both SPF KD-fed
184 and KD-CMT mice exhibited a higher number of less abundant genes/Pfams than more abundant
185 genes/Pfams, suggesting a KD-induced functional depletion (Extended Data Fig. 7e (SPF, KEGG), 7f (CMT,
186 KEGG), 7g (CMT, KEGG) and 7h (CMT, Pfam)). Accordingly, gene set enrichment (Fig. 3d and Extended Data

187 Fig. 7i) and overrepresentation analysis (Fig. 3e) of identified KEGG orthologs revealed differences in
188 carbohydrate metabolism between the treatment groups in the SPF diet and CMT experiments, such as
189 reduced starch and sucrose metabolism under ketogenic conditions. In line with this, genes assigned to
190 Pfams associated with carbohydrate metabolism accounted for a large proportion of over- and under-
191 represented genes under ketogenic conditions (Extended Data Fig. 7j (SPF) and Extended Data Fig. 7k
192 (CMT)). Furthermore, we found differential abundance of several CAZymes between dietary conditions,
193 which are known to play a crucial role in the building and breaking down of complex carbohydrates for
194 use by the organism[20], with an overall increase in glycosyltransferases (GT; Extended Data Fig. 7l). Filtering
195 the SPF diet and CMT datasets for KEGGs, Pfams and CAZymes, which were simultaneously enriched or
196 depleted, yielded a list of 15 genes with varying functions, of which five were more abundant and ten
197 were less abundant in ketogenic conditions (Extended Data Fig. 7m, Supplementary Table 5). Altogether,
198 this data underlines the selective pressure of the KD on the gut microbiome, and its capacity to shape
199 long-term overall gut microbial function.
200

201 **The microbial metabolite stearate is elevated in ketogenic conditions and exhibits anticancer**
202 **effects**

203 In order to investigate the link between functional alterations of the gut microbiome and the
204 observed cancer phenotype, we investigated fecal metabolic profiles. Analysis of fecal metabolites
205 revealed distinct clustering of samples by condition in both the SPF dietary and CMT experiments (Fig. 4a
206 and 4b, respectively). Mice in the ketogenic conditions presented altered amino acid, fatty acid,
207 carbohydrate and SCFA profiles (Supp. Tables 6 and 7), albeit to a lesser extent in the CMT experiment. A
208 single detected long-chain fatty acid, namely octadecanoic acid (also known as stearic acid), was elevated
209 in KD (Fig. 4c) and KD-CMT (Fig. 4e) mice. Strikingly, stearic acid levels correlated with colonic tumor
210 burden in the SPF dietary experiment (Fig. 4e), with a similar trend observed in the CMT experiment,

211 suggesting a functional relevance of long-chain fatty acid metabolism in CRC. In addition, associations
212 between the abundances of all identified KEGG orthologs and tumor counts in the SPF dietary experiment
213 identified a correlation between colonic tumor burden and some lipid-metabolism-associated KEGGs,
214 such as FabH, 3-oxoacyl-[acyl-carrier-protein] synthase III (K00648), FabB, 3-oxoacyl-[acyl-carrier-protein]
215 synthase I (K00647), FabZ, 3-hydroxyacyl-[acyl-carrier-protein] dehydratase (K02372), and FabF, 3-
216 oxoacyl-[acyl-carrier-protein] synthase II (K09458) (Fig. 4f and Extended Data Fig. 8a). Indeed, core fatty
217 acid biosynthesis KOs (Extended Data Fig. 8b) were less abundant in the ketogenic diet group of the SPF
218 diet experiment, except for the different enoyl-carrier ACPs and the thioesterases, of which one or more
219 can be found in most bacterial genomes (Extended Data Fig. 8c). Reflecting their essential function, the
220 core enzymes of the fatty acid synthesis pathway correlating with tumor counts were found in both
221 Bacteroidetes and Firmicutes genomes. In KD, contigs carrying K00647, K00648, K09458 and K02372 were
222 assigned to *Akkermansia* spp., *Flavonifractor* spp. and uncharacterized Firmicutes genera, whereas many
223 SD contigs were assigned to Bacteroidetes genera (*Bacteroides* spp.*, Parabacteroides* spp.*, Muribaculum*
224 spp. and uncharacterized Bacteroidetes; Extended Data Fig. 8d).

225 Given that different bacterial taxa are known to produce and consume different fatty acids, which
226 are used for membrane biogenesis and as signaling molecules, we further investigated which bacterial
227 taxa may be responsible for the release of fatty acids and which bacteria may be able to uptake free fatty
228 acids. Interestingly, detection of long-chain fatty acids in different bacterial cultures (Extended Data Fig.
229 8e; re-analysis of the publicly available dataset from the Sonnenburg lab[21]), revealed that – in line with
230 the shifts in the microbial communities observed under KD (Fig. 4h and Extended Data Fig. 9f) - the
231 *Ruminococcaceae* and *Lachnospiraceae* families, both belonging to the class Clostridia, were consistent
232 producers of stearic acid, while *Tanerellaceae* and *Bacteroidaceae,* both belonging to the class
233 Bacteroidia, were consistent consumers (Fig. 4g). The *Clostridiaceae* family was composed of both
234 producers and consumers of stearic acid (Fig. 4g). Importantly, acyl-CoA thioesterase I TesA (K10804), a

key thioesterase responsible for the release of fatty acids from their acyl carrier, alongside the fatty acid kinase FakA (K07030) used by Gram-positive bacteria to activate exogenous fatty acids, were inversely correlated with colonic tumor burden in the SPF dietary experiment (Fig. 4i). A larger proportion of K10804 was assigned to Clostridia in the ketogenic condition, and Bacteroidia in the standard condition in both experiments (Fig. 4i), indicating that the lower levels of luminal stearate detected in standard conditions may be due to the increased abundance of Bacteroidia, which, although they harbor the gene for fatty acid release, are known stearate consumers[21]. K07030 was largely attributed to Clostridia and other Firmicutes (Fig. 4i), suggesting that these bacteria can uptake exogenous fatty acids (for example from the ketogenic diet) and might further elongate them into other long-chain fatty acids for downstream use or release. The observed contrast between the abundance of fatty acid release KOs and actual production/consumption of stearic acid by different bacteria as detected in the Sonnenburg dataset suggests that different bacteria contribute differently to the overall fatty acid pool. Therefore, despite no difference in the overall abundance of K10804 and K07030 between dietary conditions (Extended Data Fig. 8c), when assigned to stearate-producing bacterial families (as detected in the Sonnenburg dataset), these KOs may result in increased levels of stearate, as in the ketogenic conditions, while when assigned to stearate-consuming families, they may result in a decrease in stearate levels. To assess the putative anti-cancer properties of the long-chain fatty acid of interest identified in the dietary and CMT experiments, we treated various CRC cell lines with increasing concentrations of stearic acid. We observed a dose-dependent reduction in cell growth (Fig. 4j, 4k, 4l, Extended Data Fig. 8g, 8h, 8i), highlighting stearic acid as an anti-cancer metabolite.

Altogether, these results suggest that KD consumption can lead to lasting functional effects on the gut microbiome, affecting the bacterial secretome, and persisting even when the selective pressure of the KD itself is no longer present.

259 **Discussion**

260 In this study we identified the gut microbiome as a driving factor in the anti-cancer effect of KD in
261 CRC. We observed that KD alters gut microbial function, namely bacterial carbohydrate metabolism and
262 the fatty acid pool. Upon KD consumption and following microbial transplantation, we observed an
263 increase in fecal octadecanoic acid, a long-chain fatty-acid, which exhibited anti-cancer properties *in vitro*.

264 The anticancer properties of the ketone body β-HB have been reported in several instances[3,4],
265 however, we observed the absence of a KD-induced anticancer effect in the absence of robust gut
266 microbial changes, despite confirmed induction of ketosis in these mice. Thus, ketosis alone seems to be
267 insufficient to ensure CRC suppression, similarly to other studies showing no KD benefits in the context of
268 cancer, despite the induction of ketosis[3,22].

269 Our results instead suggest that the anti-cancer effect of KD is based on gut microbial function,
270 rather than composition. The importance of microbial function rather than microbial composition of the
271 intestinal flora can be observed in other contexts as well. In melanoma, three different studies
272 demonstrated that the microbiome was responsible for ensuring the response to checkpoint inhibitor
273 therapy[23–25]. Interestingly however, these studies highlighted distinct bacterial species underlying this
274 response, suggesting that microbiome-encoded functions rather than individual bacterial species are
275 important in driving therapy response.

276 In regard to our own study, the depletion of dietary carbohydrates is known to provide a growth
277 advantage for certain bacteria, such as *Alistipes* spp., *Bilophila* spp. and mucin-degraders like *Akkermanisa*
278 spp., whereas *Bifidobacterium* spp. and some *Bacteroides* spp. are typically depleted[5,26], most likely due
279 to their preference for dietary carbohydrates over host glycans[27–29]. The shift from taxa dependent on
280 dietary carbohydrates taxa to taxa able to use alternative energy sources is reflected in the CAZyme profile
281 shift in KD and KD-CMT mice. For instance, the glycosylhydrolase GH101, enriched in all three of our
282 metagenomic datasets, is mucin-specific, and is required to cleave core-1 *O*-linked glycans[30]. In contrast,

283 the glycosylhydrolases GH50, present in the genomes of many *Bacteroides* spp. and *Proteobacteria* spp.,
284 and GH128, amongst others present in the genomes of the strongly reduced *CAG-485* and *CAG-873*
285 members, are specific for dietary carbohydrates[31] and accordingly found in reduced abundance following
286 KD intervention. These specific effects clearly demonstrate how diet systematically shapes the taxonomic
287 composition of the microbiome, driven and accompanied by a functional adaptation of the microbiome
288 to the new environment.

289 Although still an ongoing debate, the link between mucin-degrading bacteria and gut barrier
290 function is well-described. While overgrowth of mucin-degrading bacteria are known to damage the
291 epithelium[32], microbial mucin metabolism is considered beneficial as it is known to change the
292 glycosylation profile of the intestine[33,34], and increase mucin turnover[35]. Indeed, no mucus thinning could
293 be observed in KD-fed mice.

294 Analysis of the fecal metabolomes in the dietary intervention and CMT experiments identified
295 differences in the fatty acid pool. Amongst others, microbiome-derived fatty acids have an
296 immunomodulatory potential[36,37]. Interestingly, both *A. muciniphila* and *R. gnavus* produced higher levels
297 of palmitic and stearic acid when grown in the presence of mucins, linking bacterial fatty acid metabolism
298 to mucin physiology. In addition to their essential role in membrane biogenesis, fatty acids produced by
299 bacteria have signaling functions and play an essential role in host-microbe interactions[36]. The fatty acid
300 profile is highly species-, or even strain-, and substrate-dependent and various microbial-derived fatty
301 acids have different effects linking bacterial fatty acid metabolism to host health and disease[36].

302 Stearic acid, a long-chain fatty-acid, can originate from the diet, the host[38] and the gut
303 microbiome[39]. Stearic acid is normally desaturated by the host enzyme SDC1[40], is downregulated upon
304 reduced glucose intake and has been linked to inflammation[41–43]. Recently, Kindt et al. showed that
305 microbiome-derived acetate activated SDC1 and promoted fatty acid desaturation[44]. Furthermore, certain
306 members of the gut microbiome can directly affect stearic acid levels by consuming it as an exogenous

307 fatty acid for membrane lipid synthesis[21], producing it *de novo*[45], transforming it from oleic acid, or as a
308 product of mono- and polyunsaturated acid degradation[46,47]. In our experiments, as fecal stearic acid
309 levels were increased not only upon KD consumption, but also in KD-CMT, it is likely that the shift in the
310 microbial community is contributing to the changes in the fatty acid pool. Importantly, potential stearate-
311 producing members were enriched by the KD, whereas consumers were depleted (Fig. 4g and 4h).

312 Furthermore, several studies investigating the properties of stearic acid have demonstrated its
313 anti-cancer effects, both *in vitro* and *in vivo*. Stearic acid inhibited colony formation in different human
314 cancer cell lines[48], reduced tumor burden in rat model of mammary carcinoma[49], possibly by inducing
315 apoptosis via signaling through protein kinase C[50]. Finally, a recent study was able to not only validate the
316 suppression of colorectal adenocarcinoma by stearic acid, but also its synergy with 5-FU treatment[51]. This
317 effect might not be limited to stearic acid and its implications for human health and CRC in particular need
318 further investigation.

319 Based on our observations in the context of this study, the gut microbiome plays a central role in
320 ensuring the anti-cancer effects of the KD in the context of a murine model of inflammation-driven CRC.
321 Nevertheless, within this experiment, we can observe a more pronounced anti-cancer phenotype for
322 some mice than for others. This might indicate that the initial gut microbiome profile may determine
323 whether an individual is a “responder” or a “non-responder” to the KD in the context of CRC. The concept
324 of “responders” and non-responders” has been explored, albeit to a relatively limited extent, in epilepsy
325 patients who undergo KD therapy for the reduction of seizures[52]. Furthermore, the response to some
326 cancer treatments, such as immune checkpoint inhibition depend on gut microbial composition[53], and
327 ketogenic dietary regimens may be able to enhance the effects of these therapies[8]. Future studies
328 identifying biomarkers to predict response to dietary intervention based on the resident gut microbiome
329 and studies aiming to transform a “non-responder” microbiome into a “responder” microbiome would be
330 a significant step forward towards personalized patient care.

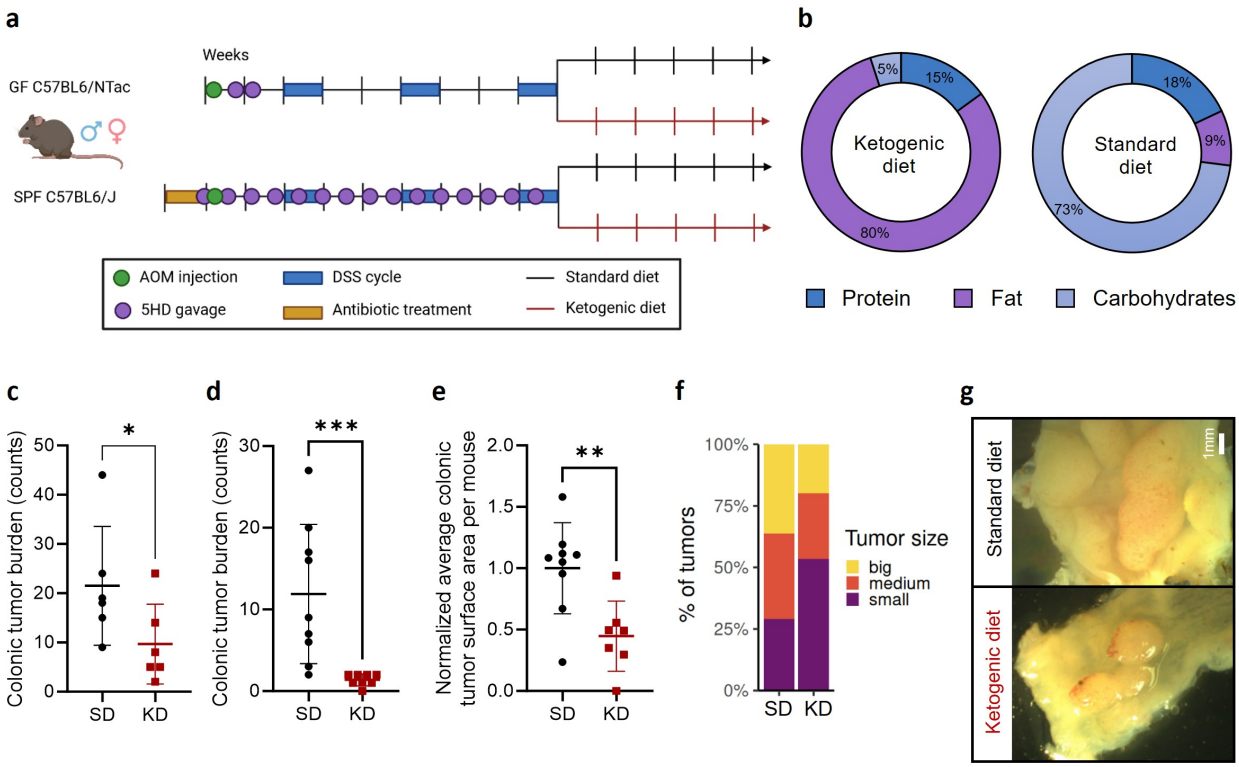

Figure 1. Ketogenic diet leads to lower colonic tumor incidence and smaller tumor size in an inflammatory model of CRC. | a. Schematic representation of the dietary AOM/DSS experimental setup in the GF (top) and SPF (bottom) facilities (created with BioRender.com). **b.** Compositions of the KD and SD, with % of calories from the indicated source. **c.** Colonic tumor burden in GF KD- and SD-fed mice. **d-f.** Colonic tumor burden (**d**), normalized average colonic tumor surface area per mouse (**e**) and tumor surface area distribution (small= first tertile, medium=second tertile, big=third tertile; Chi-squared test $\chi 2$ (2, N = 87) = 3.4, p = 0.184; **f**) in SPF KD- and SD-fed mice. Data in (**c**) shows n=6 mice per condition from one experiment. Data shows n=8 and 9 mice in the KD-fed condition and the SD-fed conditions respectively, pooled from two independent experiments in the SPF facility. Two-tailed Mann-Whitney test, **p<0.01, ***p<0.001. **g.** Representative images of the distal portion of the colon from one KD- and one SD-fed mouse in the SPF facility. Scale bar = 1mm.

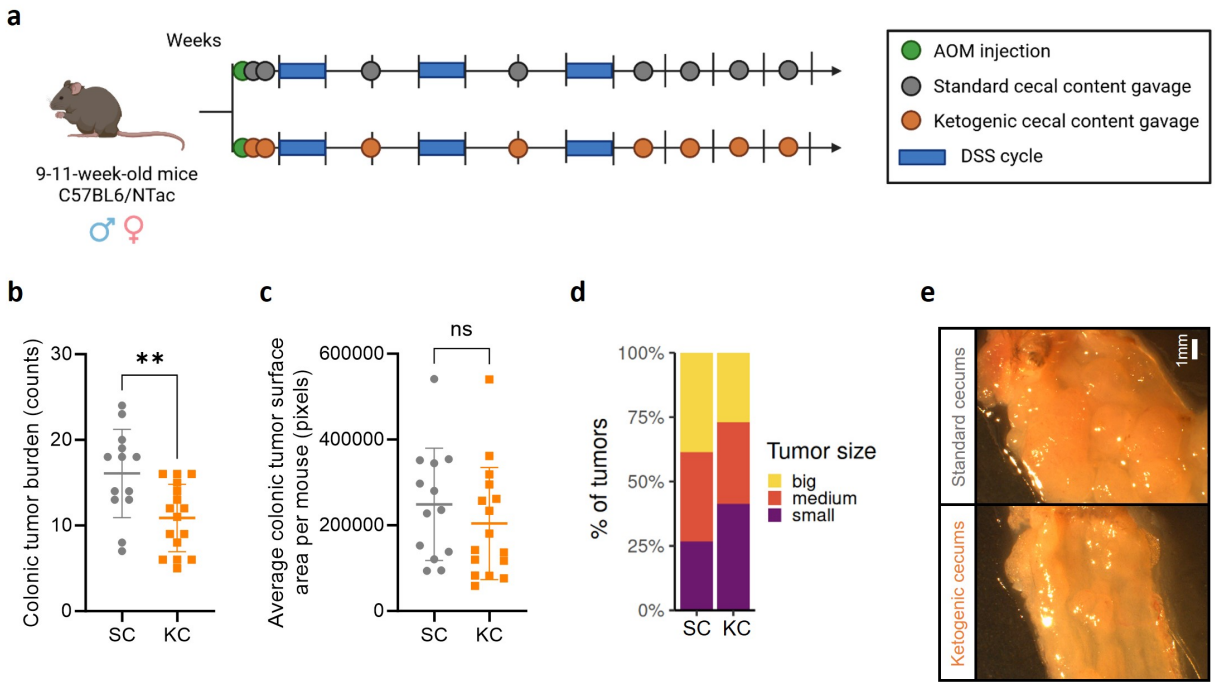

Figure 2. The tumor-inhibitory effect of ketogenic diet is mediated by the gut microbiome. | a. Schematic representation of the cecal microbial transfer experimental setup in the GF facility (created with BioRender.com). **b-e.** Colonic tumor burden (**b**), average colonic tumor surface area per mouse (in pixels) (**c**), and tumor surface area distribution (small= first tertile, medium=second tertile, big=third tertile; Chi-squared test $\chi 2$ (2, N = 384) = 10.3, p = 0.00586; **d**), in KC and SC recipient mice. n=16 KC recipient mice and n=13 SC recipient mice. Cecal matter from n=8 different donor mice per condition was used for CMT. Data shown as mean±SD in (**b**) and (**c**). Two-tailed Mann Whitney U test, **p<0.01, ***p<0.001 in (**b**) and (**c**). **e.** Representative images of the distal portion of the colon from one KC and SC recipient mouse. Scale bar = 1mm.

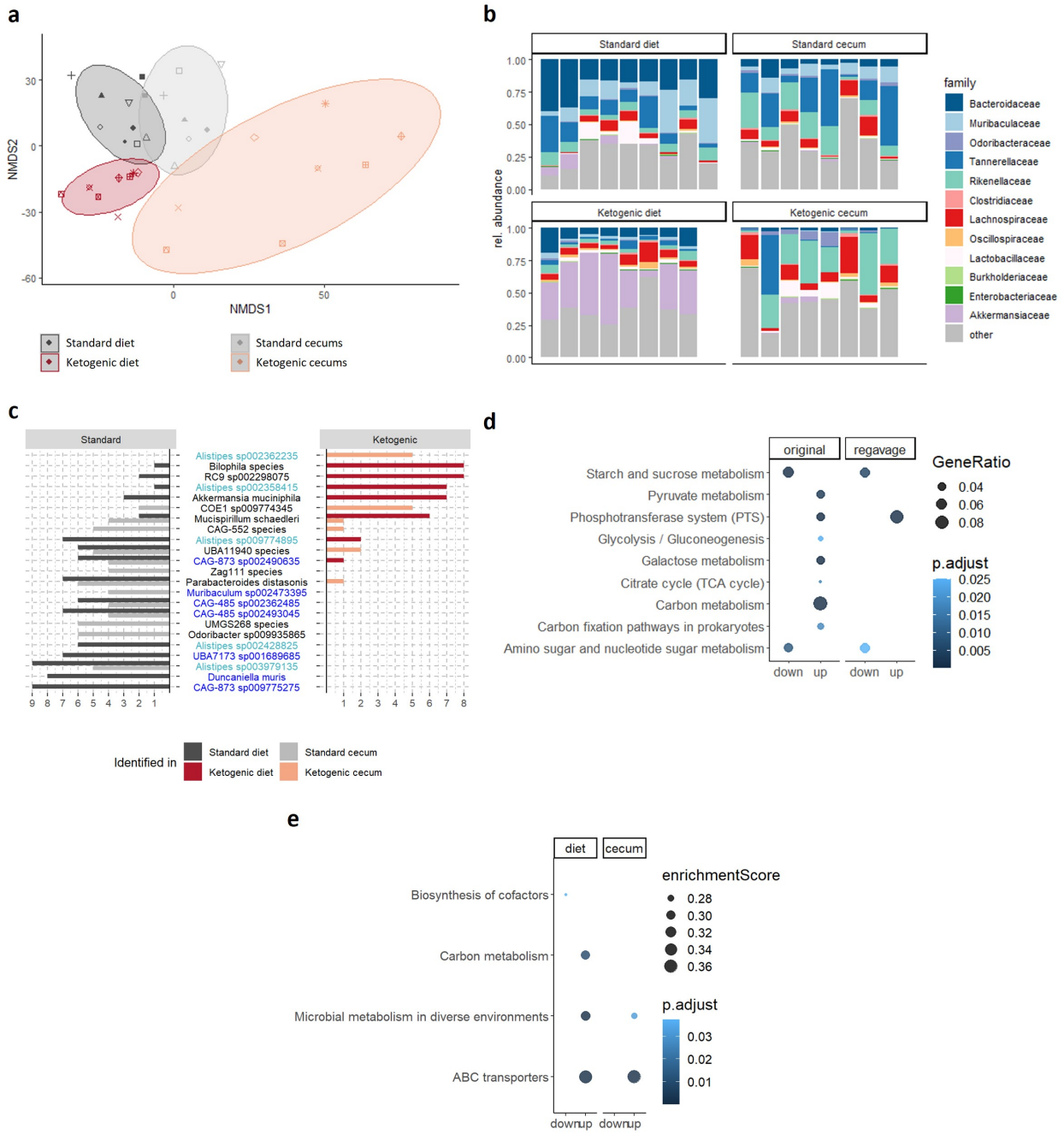

Figure 3. Ketogenic diet alters gut microbiome composition and functions. | a-c. β-diversity as assessed by NMDS (95% confidence interval) of Euclidean distance (**a**), relative abundance of bacterial families (**b**), and highly characteristic bacterial MAGs (detected in at least six mice in one condition but not more than three mice in the other (diet experiment); detected in at least four mice in one condition but not more than three mice in the other (CMT experiment), **c**) detected in KD, SD, KC and SC murine fecal samples at

363 endpoint, as analyzed by WGS. In (**c**), *Rikenellaceae* are highlighted in light blue and *Muribaculaceae* in
364 dark blue. **d-e.** Overrepresentation (KEGG, input threshold log2FC > 2, **d**) and gene set enrichment analysis
365 (GSEA, KEGG) of differentially abundant genes (threshold p.adj. < 0.05, **e**) between KD, SD, KC and SC fecal
366 samples at endpoint. In (**d**), data point size corresponds to gene ratio. Data shows results from n=8 SPF
367 KD-fed mice, n=9 SPF SD-fed mice, pooled from two independent experiments, and n=8 KC and n=8 SC
368 mice from one experiment.

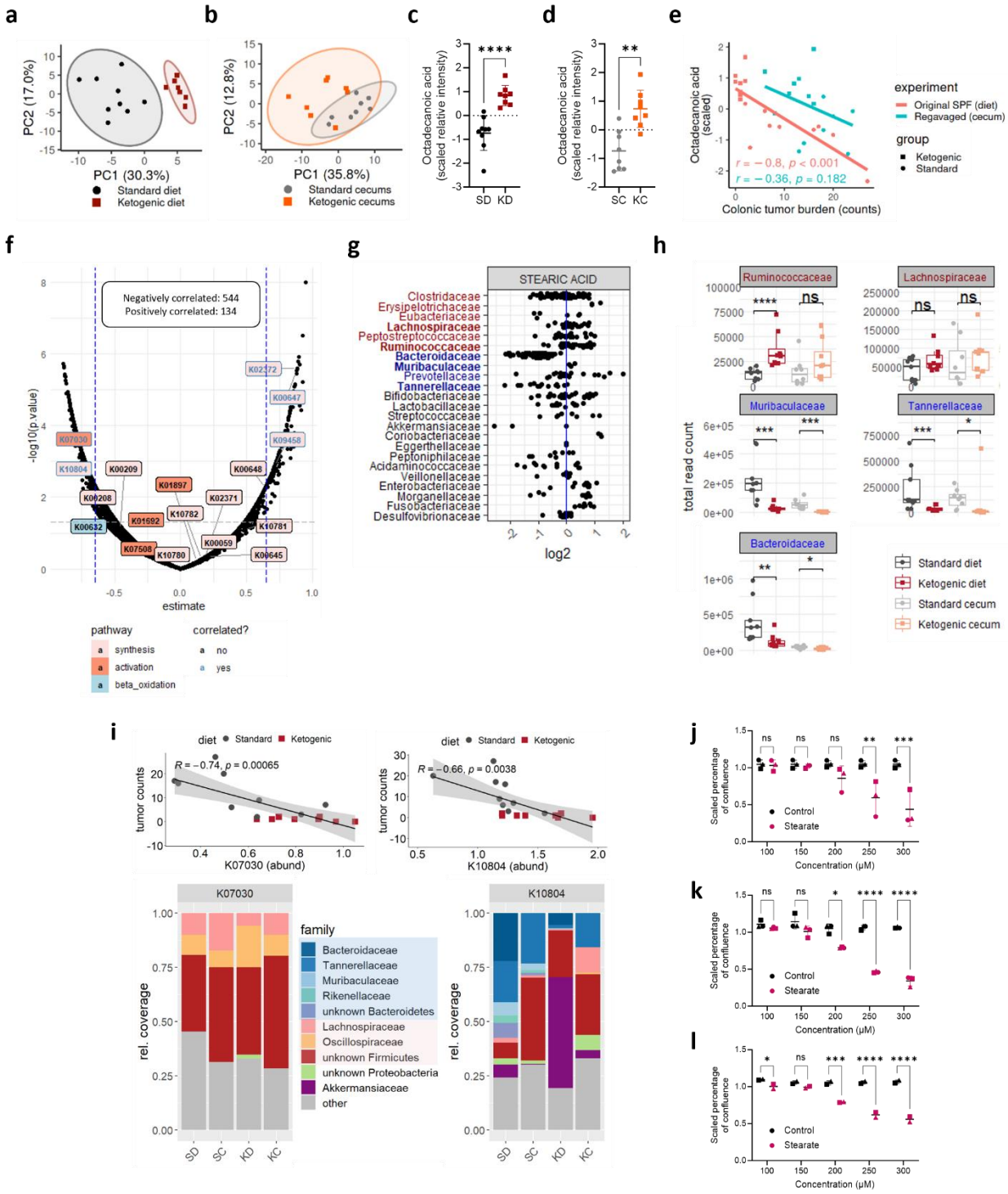

369

370 **Figure 4. The microbial metabolite stearate is elevated in ketogenic conditions and exhibits anticancer**

371 **effects. | a-b.** PCA (95% confidence interval) of identified metabolites from fecal samples from SPF KD-

372 and SD-fed mice (**a**) and from KC and SC recipient mice (**b**), as analyzed by united GC-MS and LC-MS. **c-d.**

373 Scaled octadecanoic acid (stearic acid) levels detected in fecal samples from SPF KD- and SD-fed mice(**d**)
374 and from KC and SC recipient mice (**e**), as detected by LC-MS. **e.** Correlation of colonic tumor burden with
375 fecal octadecanoic acid levels in SPF KD- and SD-fed mice (red) and in KC and SC recipient mice (blue).
376 Two-sided Pearson correlation testing was used. **f.** Correlation analysis (Pearson) between KO abundance
377 and colonic tumor burden in KD- and SD-fed mice. Vertical blue dotted lines represent thresholds for
378 correlation coefficients (r) above and below 0.65 and -0.65, respectively. The horizontal gray dotted line
379 represents the threshold for statistical significance -log10(0.05). KOs involved in fatty acid metabolism
380 appear labelled on the volcano plot and are represented in different colors (pink=synthesis,
381 orange=activation and blue=β-oxidation). Of those, significantly correlated KOs are labelled in light blue
382 font. **g.** Levels of stearic acid measured in bacterial cultures (in relation to sterile growth medium, shown
383 as $\log_2$) of the Sonnenburg dataset. Members of the class Clostridia are listed in red, while members of
384 the class Bacteroidia are listed in blue. Total read counts detected in murine fecal samples from KD-, SD-
385 fed, KC and SC recipient mice at endpoint of members listed in bolded text are shown in (**h**). **h.** Relative
386 abundance (total read counts) of stearate-producing and -consuming families of interest detected in
387 murine fecal samples from KD-, SD-fed, KC and SC recipient mice at endpoint selected from (**g**). **i.**
388 Correlation (Pearson) between colonic tumor burden and the selected KOs of interest K07030 and K10804
389 (**top**); Relative taxonomic assignment of contigs encoding for the selected KOs of interest K07030 and
390 K10804 at family level (**bottom**) detected in murine fecal samples from KD-, SD-fed, KC and SC recipient
391 mice at endpoint. Members of the class Bacteroidia are shaded in blue, while members of the class
392 Clostridia are shaded in red. **j-l.** Scaled HCT 116 (**j**), HT29 (**k**) and Caco2 (**l**) confluence at 72 hours after
393 treatment with stearic acid or corresponding controls (100µM, 150 µM, 200 µM, 250 µM, 300 µM). Data
394 shows n=3 (for HCT116 and HT29) and n=2 (for Caco2) independent experiments (indicated by different
395 datapoint shapes), each with eight technical replicates per condition. Two-sided Mann-Whitney test in (**c**)
396 and (**d**); Wilcoxon signed-rank test with Bonferroni correction in (**f**); ns $p > 0.05$, * $p \leq 0.05$, ** $p \leq 0.01$,

397 *** p ≤ 0.001, **** p ≤ 0.0001. Two-way ANOVA with multiple comparisons in (**j**), (**k**) and (**l**); **p<0.01,

398 ***p<0.001. Data shown in (**a**), (**c**), (**e, red**), (**f**), (**h, red and black**) and (**i**) are from n=9 SPF SD-fed and n=8

399 SPF KD-fed mice, pooled from two independent experiments. Data shown in (**b**), (**d**), (**e, blue**) and (**h, gray**

400 **and orange**) are from n=8 mice per condition.

401

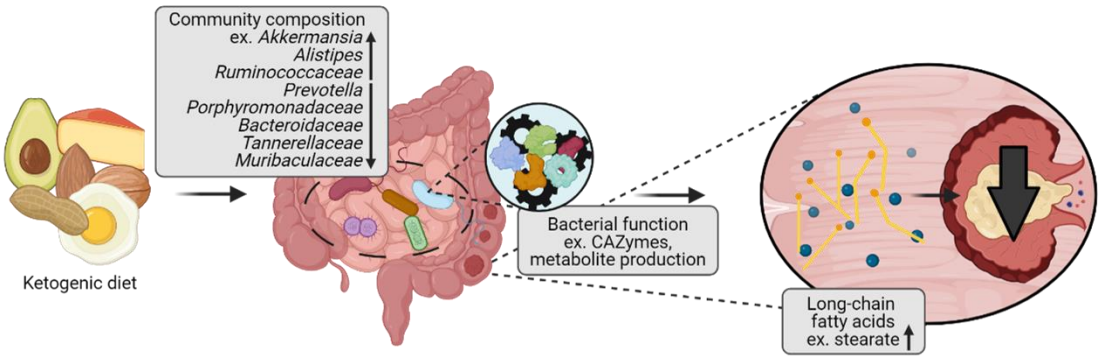

402

403 **Figure 5. Functional ketogenic-diet-induced changes in the gut microbiome are responsible for its anti-**

404 **cancer properties.**

405 Ketogenic diet consumption leads to lasting functional changes in the gut microbiome, such as alterations

406 in bacterial energy metabolism and in the long-chain fatty acid pool. The altered gut microbiome is

407 sufficient to reduce CRC development.

408

409

410

411

412

a

Donor number	1	2	3	4	5	6
Condition	Healthy	Healthy	Healthy	Healthy	Healthy	CRC
Gender	F	F	M	F	M	F
Age (years)	60	62	43	58	57	56
Cancer grade	N/A	N/A	N/A	N/A	N/A	G2

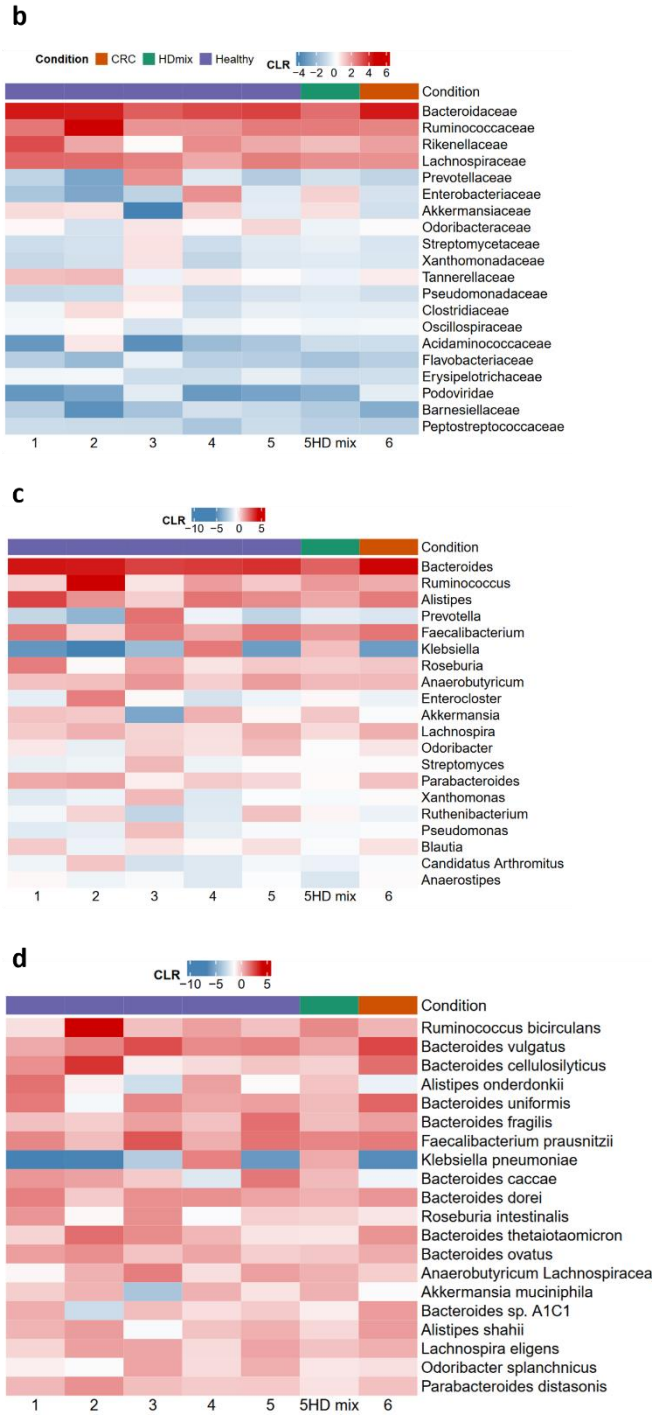

Extended data figure 1. | a. Metadata of fecal sample donors. M=male, F=female, N/A=not applicable, UNKN=unknown. **b-d.** Relative abundance of the top 20 most abundant bacterial families (**b**), genera (**c**)

416 and species (**d**) in human stool samples (CLR units)**. e.** Relative metabolite levels detected in human fecal

417 samples, analyzed by untargeted LC-MS.

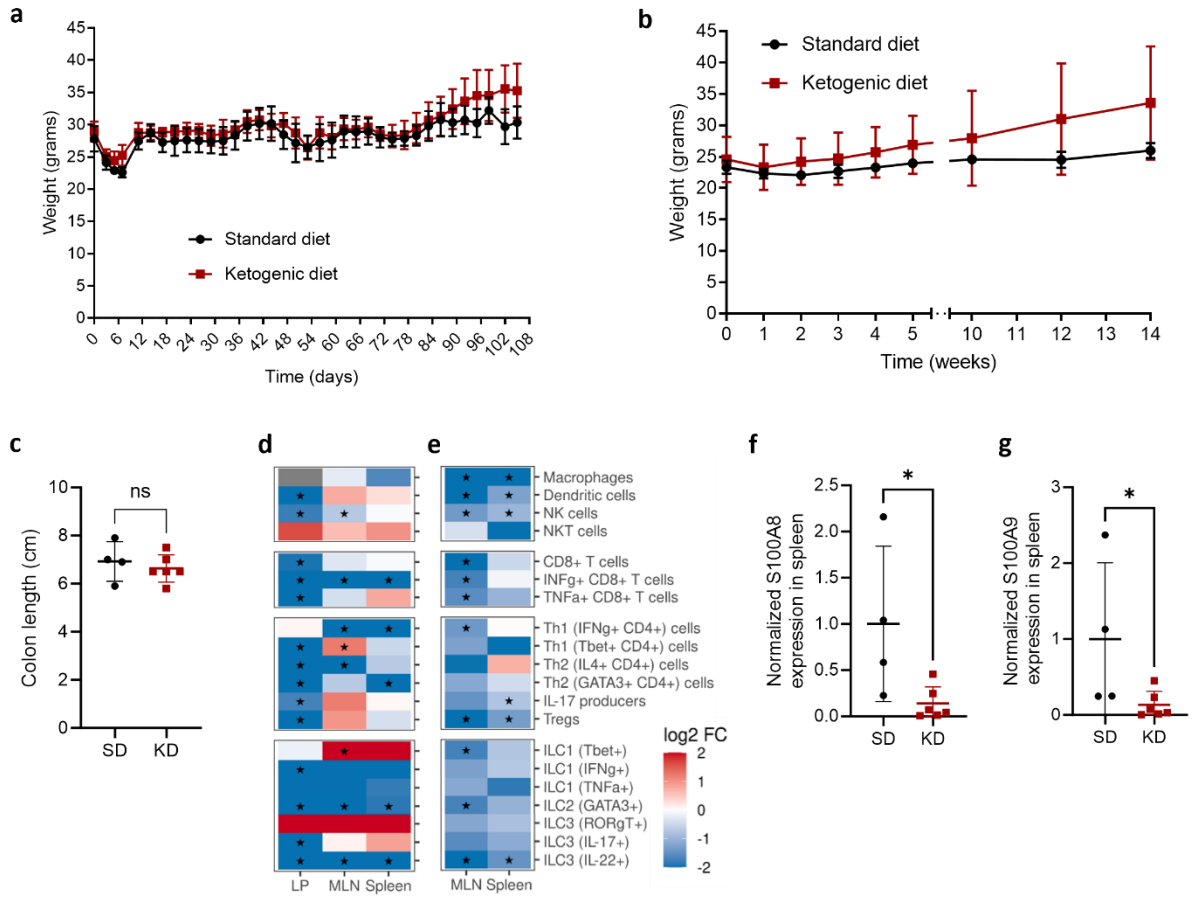

418

419 **Extended data figure 2. | a-b.** Mouse body weight (grams) over time (weeks) in the SPF (**a**) and GF (**b**)

420 dietary experiments. Weight was not recorded between week five and ten as no scale was available in the

421 facility. **c.** Colon length (cm) in the GF dietary experiment at experimental endpoint. **d-e.** Heatmap of KD-

422 induced changes in the immune cell compartment in relation to SD (log2foldchange) in the SPF (**h**) and GF

423 (**i**) diet experiments. Stars overlaid on the heatmaps indicate *p<0.05, least squared means analysis. **f-g.**

424 Normalized S100A8 (**f**) and S100A9 (**g**) expression in the spleens of mice from the GF diet experiment, as

425 determined by qPCR. Data is shown as mean±SD in (**a**), (**b**), (**c**), (**f**), and (**g**). Mann-Whitney U in (**c**), (**f**), and

426 (**g**), * p<0.05, ** p<0.01, *** p<0.001. Data in (**a**) shows n=8 and 9 mice in the KD-fed condition and the

427 SD-fed condition respectively, pooled from two independent experiments in the SPF facility. Data in (**b**),

428 (**c**), (**d**), and (**e**) shows n=4 mice in the SD-fed condition and n=6 mice in the KD-fed condition from one

429 experiment in the GF facility. Data in (**f**) and (**g**) shows n=4 mice per condition from one experiment in the

430 GF facility.

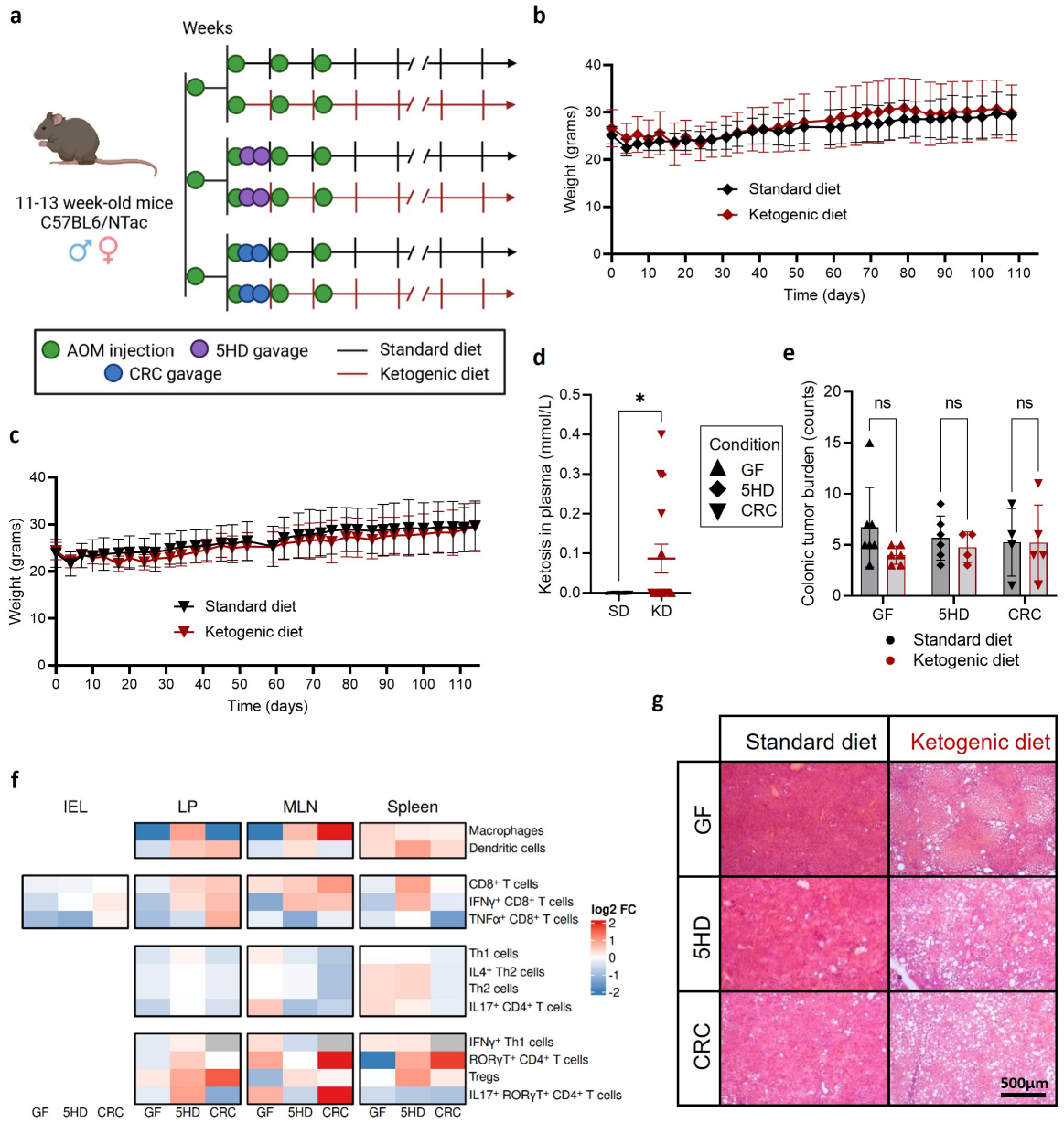

431

432 **Extended data figure 3. | a.** Schematic representation of the dietary AOM experimental setup in the GF

433 facility (created with BioRender.com). **b-c.** Mouse body weight (grams) over time (days) in mice

434 administered 5HD (**b**) and CRC (**c**). **d.** Ketosis levels in plasma (mmol/L), measured using a handheld
435 ketometer. **e.** Colonic tumor burden at endpoint. **f.** Heatmap of immune cell population phenotyping of
436 intra-epithelial lymphocytes (IEL), lamina propria (LP), mesenteric lymph nodes (MLN) and spleens of KD-
437 fed mice in relation to SD-fed mice in GF mice (GF), in mice gavaged with a mixture of stool samples from
438 five healthy donors (5HD), and in mice gavaged with stool from a single CRC patient (CRC). Least-squared
439 means analysis was performed on each combination of tissue and cell immune cell type using a linear
440 model, however no statistically significant differences were found. **g.** One representative image of a
441 section of liver stained with H&E per condition. Scale bar=500µm. Data in (**b**), (**c**), (**d**) and (**e**) shown as
442 mean±SD. Mann-Whitney U test in (**d**) and (**e**), not significant (ns), * $p<0.05$, ** $p<0.01$, *** $p<0.001$. Data
443 in (**b**), (**c**), (**d**), (**e**) and (**f**) shows n=7 and 6 mice in the GF SD and KD conditions respectively, n=6 and 4
444 mice in the 5HD SD and KD conditions respectively, and n=4 and 5 mice in the CRC SD and KD conditions
445 respectively.

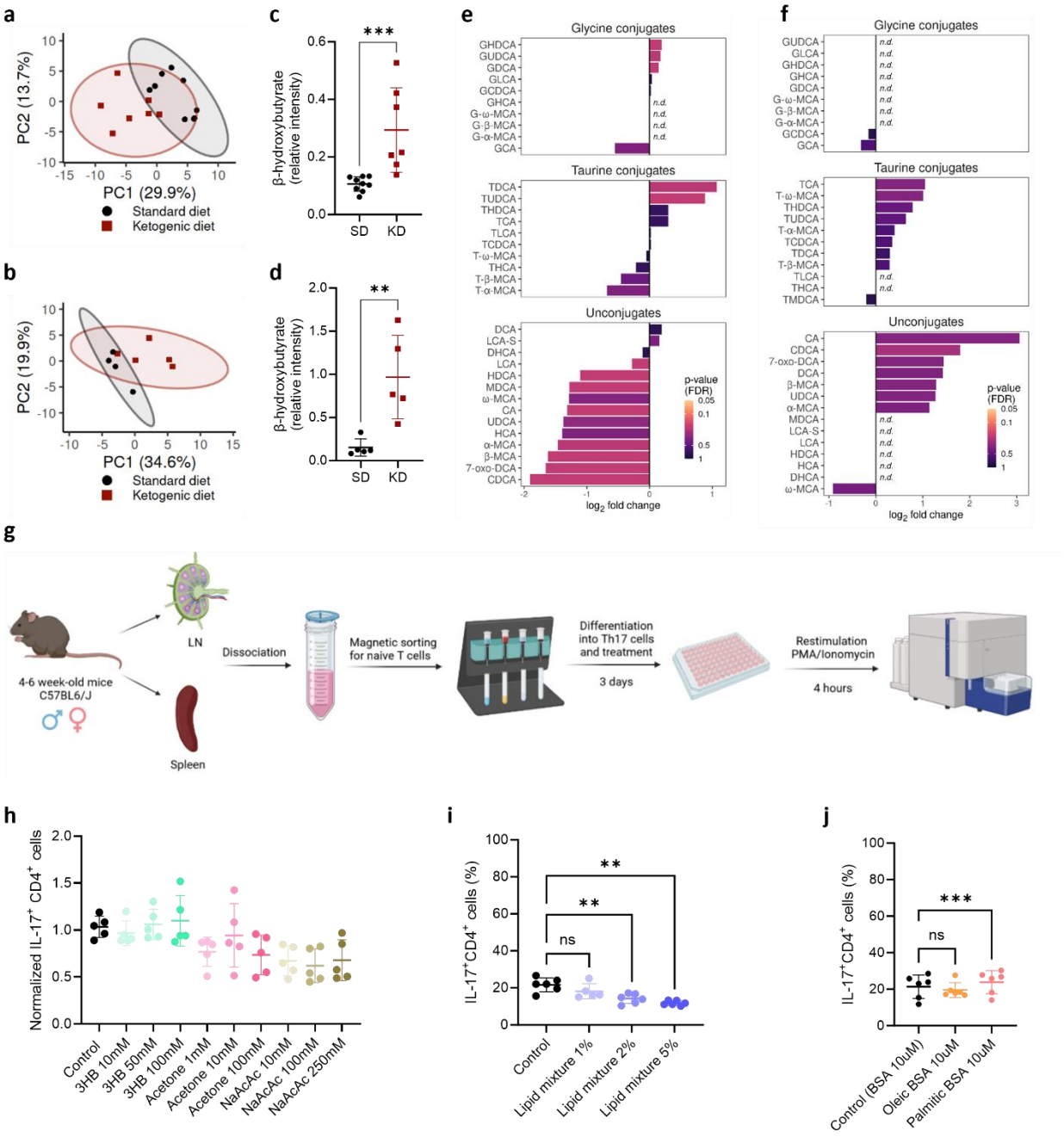

446

447 **Extended data figure 4. | a-b.** PCA (95% confidence interval) of plasma metabolites from mice in the SPF

448 (**a**) and GF (**b**) diet experiments, as analyzed by united GC-MS and LC-MS analyses (**a**) and GC-MS analysis

449 alone (**b**). **c-d.** Relative intensity of β-HB in plasma from mice in the SPF (**c**) and GF (**d**) diet experiments,

450 as analyzed by GC-MS. **e-f.** Log_2foldchange of identified plasma bile acids in KD-fed mice in relation to SD-

451 fed mice in the SPF (**e**) and GF (**f**) facilities, as analyzed UHPLC-MS. **g.** Schematic representation of the
452 experimental setup of a Th17 cell differentiation assay (created with BioRender.com). **h-j.** Th17
453 differentiation upon treatment with β-HB (10mM, 50mM, 100mM), acetone (1mM, 10mM, 100mM) or
454 sodium acetoacetate (10mM, 100mM, 250mM) in (**h**), a lipid mixture (1%, 2%, 5%) in (**i**), BSA-complexed
455 palmitic and oleic acid (10µm) in (**j**). Data in (**c**), (**d**), (**h**), (**i**) and (**j**) is shown as mean±SD. Two-tailed Mann-
456 Whitney U test in (**c**) and (**d**); Two-tailed unpaired T test with FDR correction in (**e**) and (**f**); Paired ordinary
457 one-way ANOVA in (**h**), (**i**) and (**j**); ns=not significant, * $p<0.05$, ** $p<0.01$, *** $p<0.001$. Paired ordinary
458 one-way ANOVA comparing each set of ketone body dilutions to the control yielded no statistical
459 significance in (**h**). Data in (**a**), (**c**) and (**e**) shows n=9 mice in the SD-fed condition and n=8 mice in the KD-
460 fed condition. Data in (**b**), (**d**) and (**f**) shows n=4 mice in the SD-fed condition and n=5 mice in the KD-fed
461 condition. n=6 mice in (**c**) and (**d**); n=5 mice in (**e**). Abbreviations: not detected (n.d.), cholic acid (CA),
462 hyocholic acid (HCA), chenodeoxycholic acid (CDCA), deoxycholic acid (DCA), 7-oxo-deoxycholic acid (7-
463 oxo-DCA), murideoxycholic acid (MDCA), lithocholic acid (LCA), ursodeoxycholic acid (UDCA),
464 hyodeoxycholic acid (HDCA), muricholic acids (α-MCA, β-MCA and ω-MCA), taurocholic acid (TCA),
465 taurohyocholic acid (THCA), taurochenodeoxycholic acid (TCDCA), taurodeoxycholic acid (TDCA),
466 taurolithocholic acid (TLCA), tauroursodeoxycholic acid (TUDCA), taurohyodeoxycholic acid (THDCA),
467 tauro-α-muricholic acid (T-α-MCA), tauro-β-muricholic acid (T-β-MCA) and tauro-ω-muricholic acid (T-ω-
468 MCA).

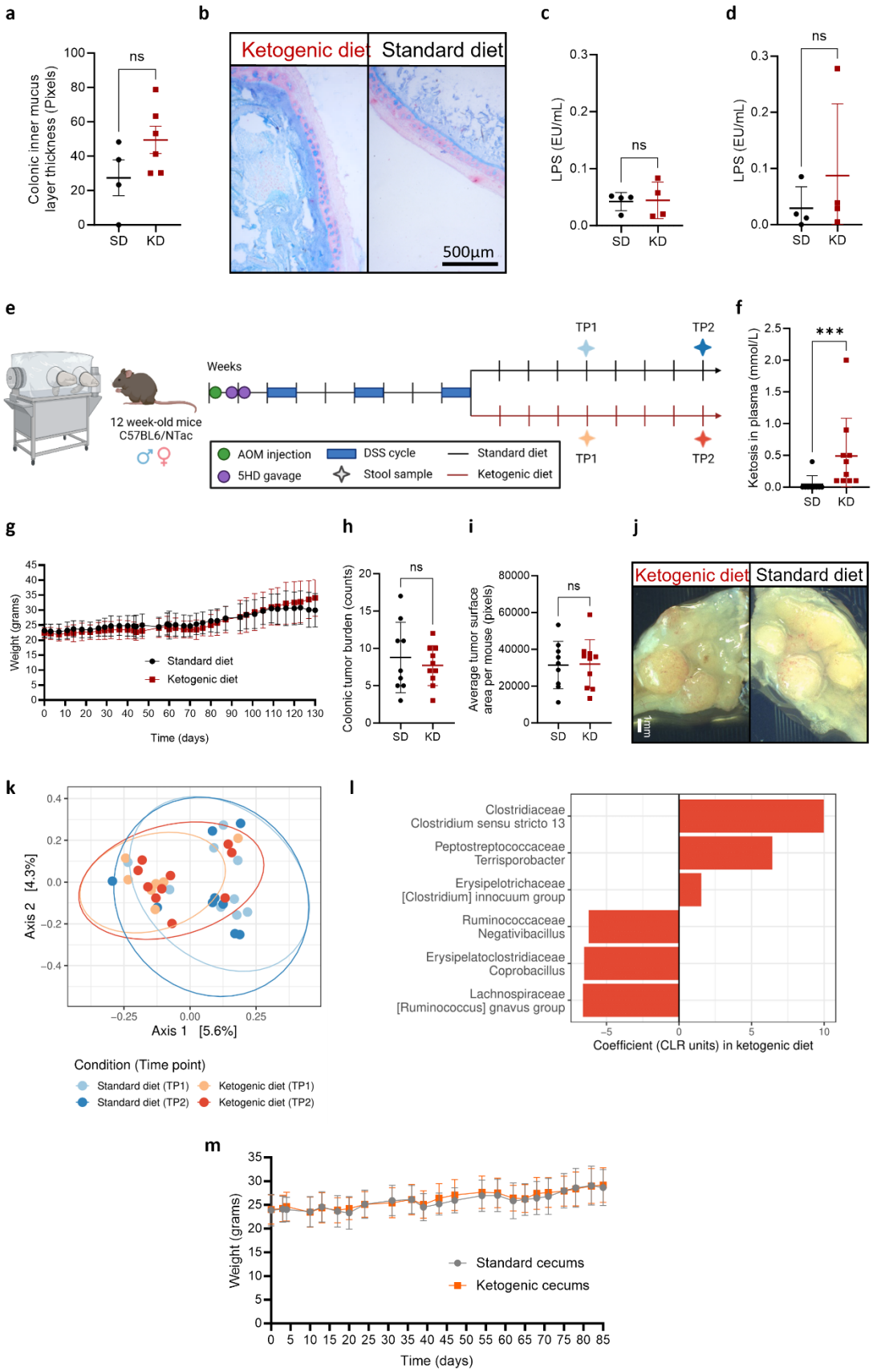
a
Colonic inner mucus layer thickness (Pixels)
ns
SD
KD
b
Ketogenic diet
Standard diet
500µm
c
LPS (EU/mL)
ns
SD
KD
d
LPS (EU/mL)
ns
SD
KD
e
12 week-old mice
C57BL6/NTac
Weeks
TP1
TP2
AOM injection
5HD gavage
DSS cycle
Stool sample
Standard diet
Ketogenic diet
f
Ketosis in plasma (mmol/L)
***
SD
KD
g
Weight (grams)
Standard diet
Ketogenic diet
Time (days)
h
Colonic tumor burden (counts)
ns
SD
KD
i
Average tumor surface area per mouse (pixels)
ns
SD
KD
j
Ketogenic diet
Standard diet
1mm
k
Axis 2 [4.3%]
Axis 1 [5.6%]
Condition (Time point)
Standard diet (TP1)
Ketogenic diet (TP1)
Standard diet (TP2)
Ketogenic diet (TP2)
l
Clostridiaceae
Clostridium sensu stricto 13
Peptostreptococcaceae
Terrisporobacter
Erysipelotrichaceae
[Clostridium] innocuum group
Ruminococcaceae
Negativibacillus
Erysipelatoclostridiaceae
Coprobacillus
Lachnospiraceae
[Ruminococcus] gnavus group
Coefficient (CLR units) in ketogenic diet
m
Weight (grams)
Standard cecums
Ketogenic cecums
Time (days)

469

Extended data figure 5. | a-b. Colonic inner mucus layer thickness (in pixels, **a**) and representative images of Alcian Blue staining of colonic cryosections (**b**) in GF KD-fed and SD-fed mice. **c-d.** LPS (endotoxin units (EU) per milliliter) in plasma from GF (**c**) and SPF (**d**) KD-fed mice and SD-fed mice measured by ELISA. Panels **a-d** relate to experiments shown in Fig. 1. **e.** Schematic representation of the experimental setup in the GF facility, in which mice were housed in open-top cages in a gnotobiotic flexible-film isolator (created with Biorender.com). **f.** Ketosis levels in mouse plasma (mmol/L), measured using a handheld ketometer. **g.** Mouse body weight (grams) over time (weeks). **h-j.** Colonic tumor burden (**h**), average tumor surface area per mouse (pixels, **i**) and representative images of colonic tumors, scale bar=1mm (**j**) from mice at experimental endpoint. **k.** β-diversity as assessed by PCoA of Bray-Curtis distance in mouse fecal samples collected at two time points. **l.** Differentially abundant bacterial families (coefficient, CLR units) in mouse fecal samples, estimated using a generalized linear model on CLR data (p.adj<0.05 (Benjamini-Hochberg correction), max. abundance>0.05), with the standard diet condition as the reference. **m.** Mouse body weight (grams) over time (days) in the CMT experiment. Data is shown as mean±SD in (**a**), (**c**), (**d**), (**f**), (**g**), (**h**), (**i**) and (**m**). Two-tailed Mann-Whitney U test in (**a**), (**c**), (**d**), (**f**), (**h**) and (**i**); * p<0.05, ** p<0.01, *** p<0.001. Data in (**a**), (**c**) and (**d**) shows n=4 mice per condition. Data in (**f**), (**g**), (**h**), (**i**), (**k**) and (**l**) shows n=9 mice in the SD-fed condition and n=8 mice in the KD-fed condition, pooled from two independent experiments. Data in (**m**) shows 16 mice per condition.

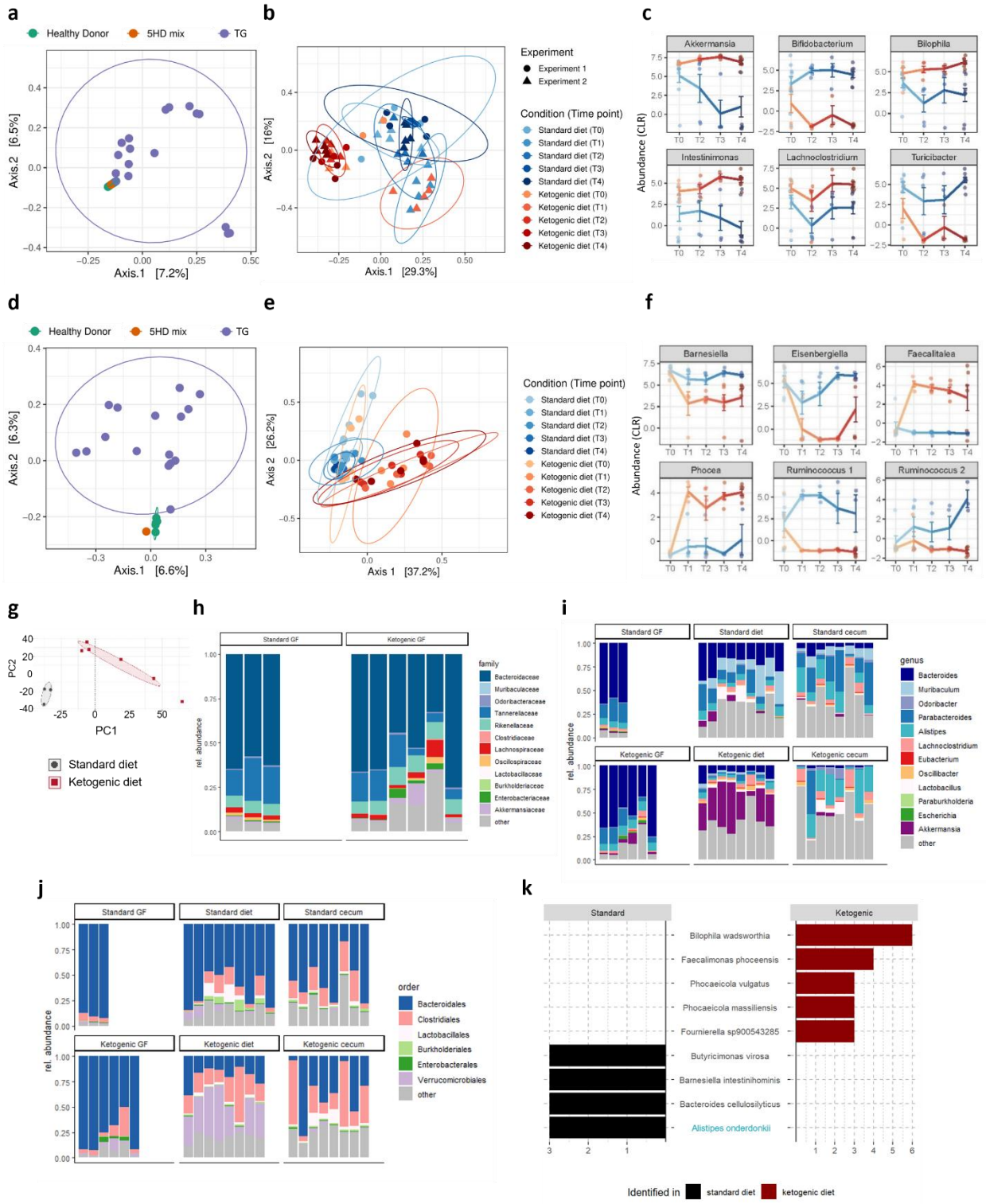

487

488 **Extended data figure 6. | a-f.** β-diversity as assessed by PCoA (95% confidence interval) of Bray-Curtis

489 distance in five individual healthy donor stool samples, in a mix of the five healthy donor stool samples

490 (5HD mix) and in murine fecal samples three days after gavage (TG, **a** and **d**); β-diversity as assessed by
491 PCoA (95% confidence interval) of Bray-Curtis distance in murine fecal samples collected over time after
492 diet change (**b** and **e**); Abundance of selected genera which are differentially abundant at at least one
493 time point (using a generalized linear model on CLR, **c** and **f**) in fecal samples collected over time after diet
494 change from SD- and KD-fed mice in the SPF (**a**, **b** and **c**) and GF (**d**, **e**, and **f**) dietary experiments (T0 at
495 diet change, T1-T4 weeks after diet change), as analyzed by 16s rRNA sequencing. **g.** PCA of WGS
496 sequencing of fecal samples collected at endpoint from GF KD and SD-fed mice. **h.** Relative abundance of
497 bacterial families (**h**) detected in fecal samples from GF KD- and SD-fed mice at endpoint, as analyzed by
498 WGS. **i-j.** Relative abundance of bacterial genera (**i**) and orders (**h**) detected in fecal samples collected at
499 endpoint from GF and SPF KD- and SD-fed mice, as well as KC and SC recipient mice, as analyzed by WGS.
500 **k.** Highly characteristic bacterial MAGs (detected in at least three mice in one condition but not more than
501 two mice in the other), detected in GF KD- and SD-fed murine fecal samples at endpoint, as analyzed by
502 WGS. Data shows samples collected from n=9 SPF SD-fed mice and n=8 SPF KD-fed mice, pooled from two
503 independent experiments in (**a**), (**b**), (**c**), (**i**) and (**j**); n= 8 KC and n=8 SC recipient mice from one experiment
504 in (**i**) and (**j**); n=3 GF SD and n=6 GF KD mice from one experiment in (**d**), (**e**), (**f**), (**g**), (**i**), (**j**) and (**k**).

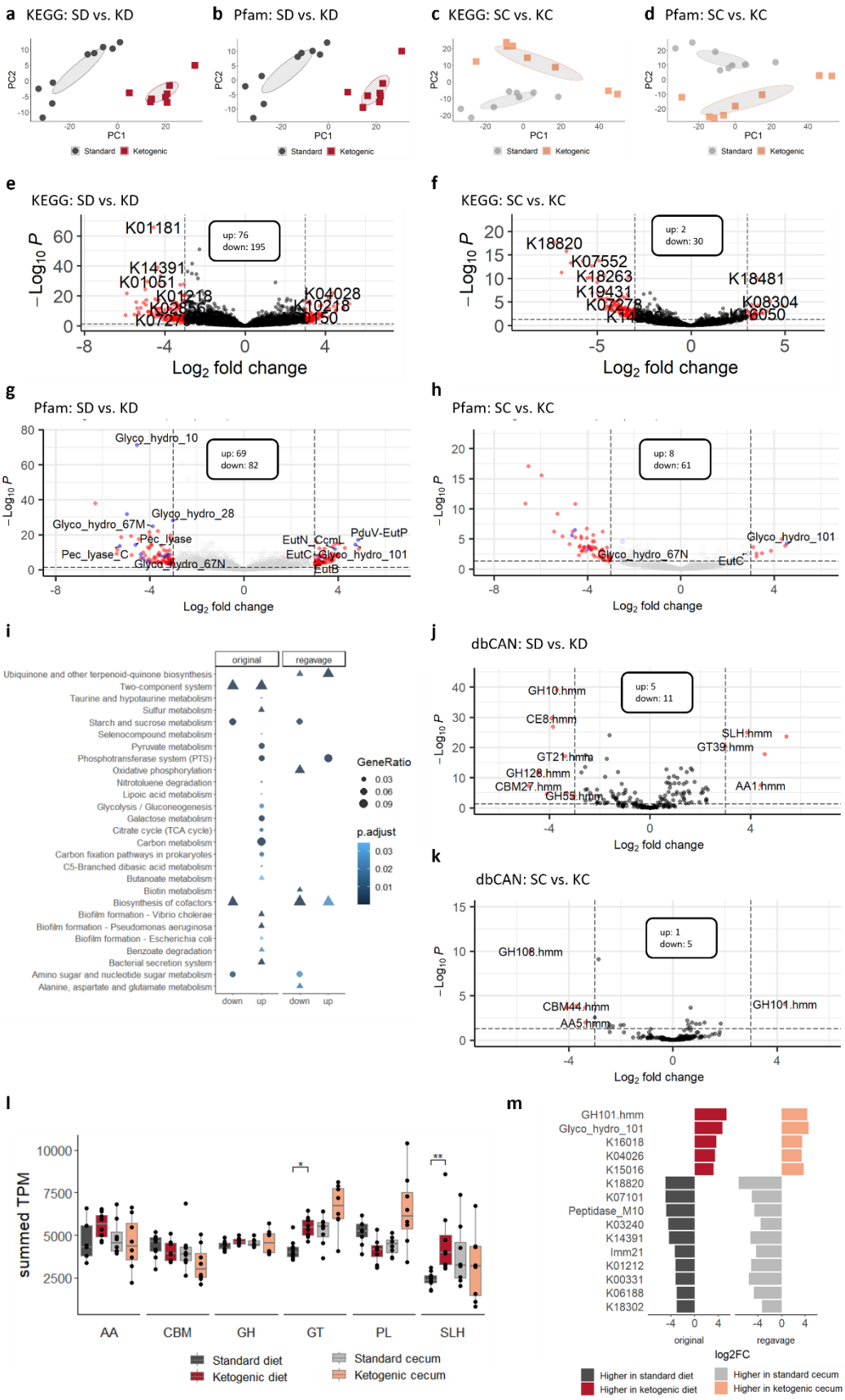
a KEGG: SD vs. KD
b Pfam: SD vs. KD
c KEGG: SC vs. KC
d Pfam: SC vs. KC
PC1
PC2
Standard
Ketogenic
e KEGG: SD vs. KD
up: 76
down: 195
K01181
K14391
K01051
K04028
K10218
f KEGG: SC vs. KC
up: 2
down: 30
K18820
K07552
K18263
K19431
K18481
K08304
g Pfam: SD vs. KD
up: 69
down: 82
Glyco_hydro_10
Glyco_hydro_28
Glyco_hydro_67M
Pec_lyase
Pec_lyase_C
Glyco_hydro_67N
EutN_CcmL
PduV-EutP
EutC
Glyco_hydro_101
EutB
h Pfam: SC vs. KC
up: 8
down: 61
Glyco_hydro_101
Glyco_hydro_67N
EutC
−Log10 P
Log2 fold change
i
original
regavage
Ubiquinone and other terpenoid-quinone biosynthesis
Two-component system
Taurine and hypotaurine metabolism
Sulfur metabolism
Starch and sucrose metabolism
Selenocompound metabolism
Pyruvate metabolism
Phosphotransferase system (PTS)
Oxidative phosphorylation
Nitrotoluene degradation
Lipoic acid metabolism
Glycolysis / Gluconeogenesis
Galactose metabolism
Citrate cycle (TCA cycle)
Carbon metabolism
Carbon fixation pathways in prokaryotes
C5-Branched dibasic acid metabolism
Butanoate metabolism
Biotin metabolism
Biosynthesis of cofactors
Biofilm formation - Vibrio cholerae
Biofilm formation - Pseudomonas aeruginosa
Biofilm formation - Escherichia coli
Benzoate degradation
Bacterial secretion system
Amino sugar and nucleotide sugar metabolism
Alanine, aspartate and glutamate metabolism
down
up
GeneRatio
0.03
0.06
0.09
p.adjust
0.03
0.02
0.01
j dbCAN: SD vs. KD
up: 5
down: 11
GH10.hmm
CE8.hmm
SLH.hmm
GT39.hmm
GT21.hmm
GH128.hmm
CBM27.hmm
GH55.hmm
AA1.hmm
k dbCAN: SC vs. KC
up: 1
down: 5
GH108.hmm
CBM44.hmm
AA5.hmm
GH101.hmm
l
summed TPM
AA
CBM
GH
GT
PL
SLH
Standard diet
Ketogenic diet
Standard cecum
Ketogenic cecum
m
GH101.hmm
Glyco_hydro_101
K16018
K04026
K15016
K18820
K07101
Peptidase_M10
K03240
K14391
Imm21
K01212
K00331
K06188
K18302
original
regavage
log2FC
Higher in standard diet
Higher in ketogenic diet
Higher in standard cecum
Higher in ketogenic cecum

505

506 **Extended data figure 7. | a-d.** PCA (95% confidence interval) of the predicted functional features of the
507 gut microbiome (KEGG, **a** and **c**) and (Pfam, **b** and **d**) of SPF KD- and SD-fed mice (**a** and **b**) and KC and SC
508 recipient mice (**c** and **d**) at endpoint. **e-h.** Differences in gene expression profiles mapped to the KEGG (**e**
509 and **f**) and Pfam (**g** and **h**) databases detected in fecal samples from KD- and SD-fed mice (**e** and **g**), and KC
510 and SC recipient mice (**f** and **h**), at endpoint. Blue data points in (**g**) and (**h**) represent carbohydrate-
511 metabolism-related Pfams, solid data points represent Pfams above both defined thresholds, while empty
512 datapoints represent Pfams below these thresholds. Pfams named in (**h**) overlap with those named in (**g**).
513 **i.** Overrepresentation analysis (KEGG, threshold log2FC > 2, p.adj. < 0.05) of genes detected in fecal
514 samples collected at endpoint from SPF KD- and SD-fed mice, and KC and SC recipient mice. Gene sets
515 related to energy metabolism are shown as circular data points, while all other gene sets are shown as
516 triangular data points. Data point size corresponds to gene ratio. **j-k.** Differences in gene expression
517 profiles mapped to the DBcan database detected in fecal samples from KD- and SD-fed mice (**j**), and KC
518 and SC recipient mice (**k**) at endpoint. **l.** Abundance of main CAZyme families (summed transcripts per
519 million (TPM)) in fecal samples from KD- and SD-fed mice, and KC and SC recipient mice, at endpoint.
520 Boxplots show medians with 1st and 3rd quantiles. The whiskers from the hinges to the smallest/largest
521 values represent 1.5*inter-quartile range (IQR). Wilcoxon signed-rank test with Holm correction in (**f**), ns
522 $p > 0.05$, * $p \leq 0.05$, ** $p \leq 0.01$, *** $p \leq 0.001$, **** $p \leq 0.0001$. Abbreviations: auxiliary activities (AA),
523 carbohydrate binding molecule (CBM), glycoside hydrolase (GH), glycosyl transferase (GT), polysaccharide
524 lyase (PL) and S-layer homology (SLH) families. **m.** Abundance (log2foldchange) of genes simultaneously
525 enriched or depleted in the KEGG, Pfam and CAZyme databases in fecal samples from SPF KD- and SD-fed
526 mice, and KC and SC recipient mice, at endpoint. In (**e**), (**f**), (**g**), (**h**), (**j**) and (**k**), the horizontal lines
527 correspond to a three-fold increase (right) or decrease (left) in KD in relation to SD, in KC in relation SC.
528 The vertical lines correspond to $p<0.05$, the defined cutoff for statistical significance (DESeq2). Red data
529 points represent statistically significantly ($p<0.05$) differentially expressed genes with three-fold up- or

530 down-regulation. Data shows n=8 SPF KD-fed mice and n=9 mice SPF SD-fed mice, pooled from two

531 independent experiments, and n=8 KC and n=8 SC recipient mice from one experiment.

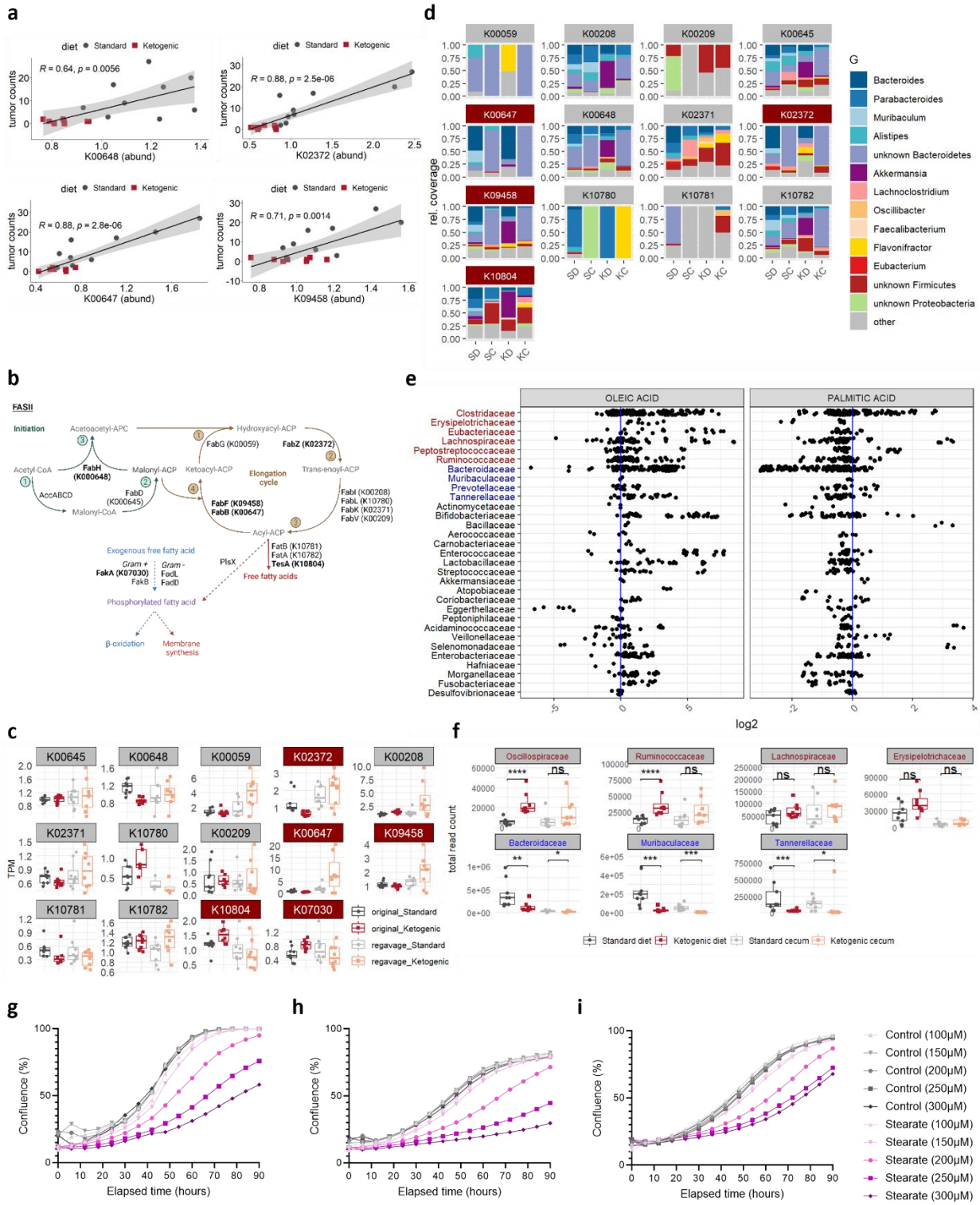

532

533 **Extended data figure 8. | a.** Correlation (Pearson) between colonic tumor burden of KD and SD-fed mice
534 and the selected KOs of interest K00647, K00648, K02372 and K09458. **b.** Schematic representation of
535 type II bacterial fatty acid synthesis created with BioRender, adapted from Yao et Rock (2017)[39]. Core
536 enzymes are shown with their corresponding KOs. The abundance of bolded KOs correlates with colonic
537 tumor burden in KD- and SD-fed mice. Abbreviations: acetyl-CoA carboxylase enzyme complex (AccABCD),
538 β-ketoacyl-ACP synthase 1 (FabB), malonyl-CoA:ACP transacylase (FabD), β-ketoacyl-ACP synthase II
539 (FabF), β-ketoacyl-ACP reductase (FabG), β-ketoacyl-ACP synthase III (FabH), enoyl-ACP reductase enzyme
540 isoforms (FabI, FabK, FabL and FabV), β-hydroxyacyl-ACP dehydratase (FabZ), long-chain-fatty-acid-CoA
541 ligase (FadD), long-chain fatty acid transport protein (FadL), fatty acid kinase (FakA, FakB), acyl-ACP
542 thioesterase (FatA), iron transport protein (FatB), thioesterase 1/protease 1/lysophospholipase L1 (TesA),
543 phosphate acyltransferase (PlsX), CoenzymeA (CoA), acyl carrier protein (ACP). **c-d.** Abundance of selected
544 KOs of interest (summed transcripts per million (TPM), **c**) and relative taxonomic assignment of contigs
545 encoding for the selected KOs of interest at genus level (**d**) in fecal samples from KD- and SD-fed mice,
546 and KC and SC recipient mice, at endpoint. In (**c**) and (**d**), the abundance of KOs highlighted in red
547 correlates with colonic tumor burden in KD- and SD-fed mice. **e.** Levels of oleic (left) and palmitic (right)
548 acid measured in bacterial cultures (in relation to sterile growth medium) of the Sonnenburg dataset. **f.**
549 Relative abundance (total read counts) of selected families of interest detected in murine fecal samples
550 from KD-, SD-fed, KC and SC recipient mice at endpoint**.** Members of the class Clostridia are listed in red,
551 while members of the class Bacteroidia are listed in blue. **g-i.** HCT 116 (**g**), HT29 (**h**) and Caco2 (**i**)
552 proliferation over time after treatment with stearic acid or control (100µM, 150 µM, 200 µM, 250 µM,
553 300 µM). Data shows mean of n=3 independent experiments (**g** and **h**), or n=2 independent experiments
554 (**i**), each with eight technical replicates per condition. In (**c**) and (**f**), boxplots show medians with 1st and
555 3rd quantiles. The whiskers from the hinges to the smallest/largest values represent 1.5*inter-quartile
556 range (IQR). Wilcoxon signed-rank test with Bonferroni correction in (**f**), ns $p > 0.05$, * $p \leq 0.05$, ** $p \leq$

557 0.01, *** $p \leq 0.001$, **** $p \leq 0.0001$. Data shown in (**a**), (**c, red and black**), (**e, red**), (**d, first and third**

558 **columns**), (**f, red and black**) and (**i**) are from n=9 SPF SD-fed and n=8 SPF KD-fed mice, pooled from two

559 independent experiments. Data shown in (**c, gray and orange**), (**d, second and fourth columns**), and (**f,**

560 **gray and orange**) are from n=8 mice per condition.

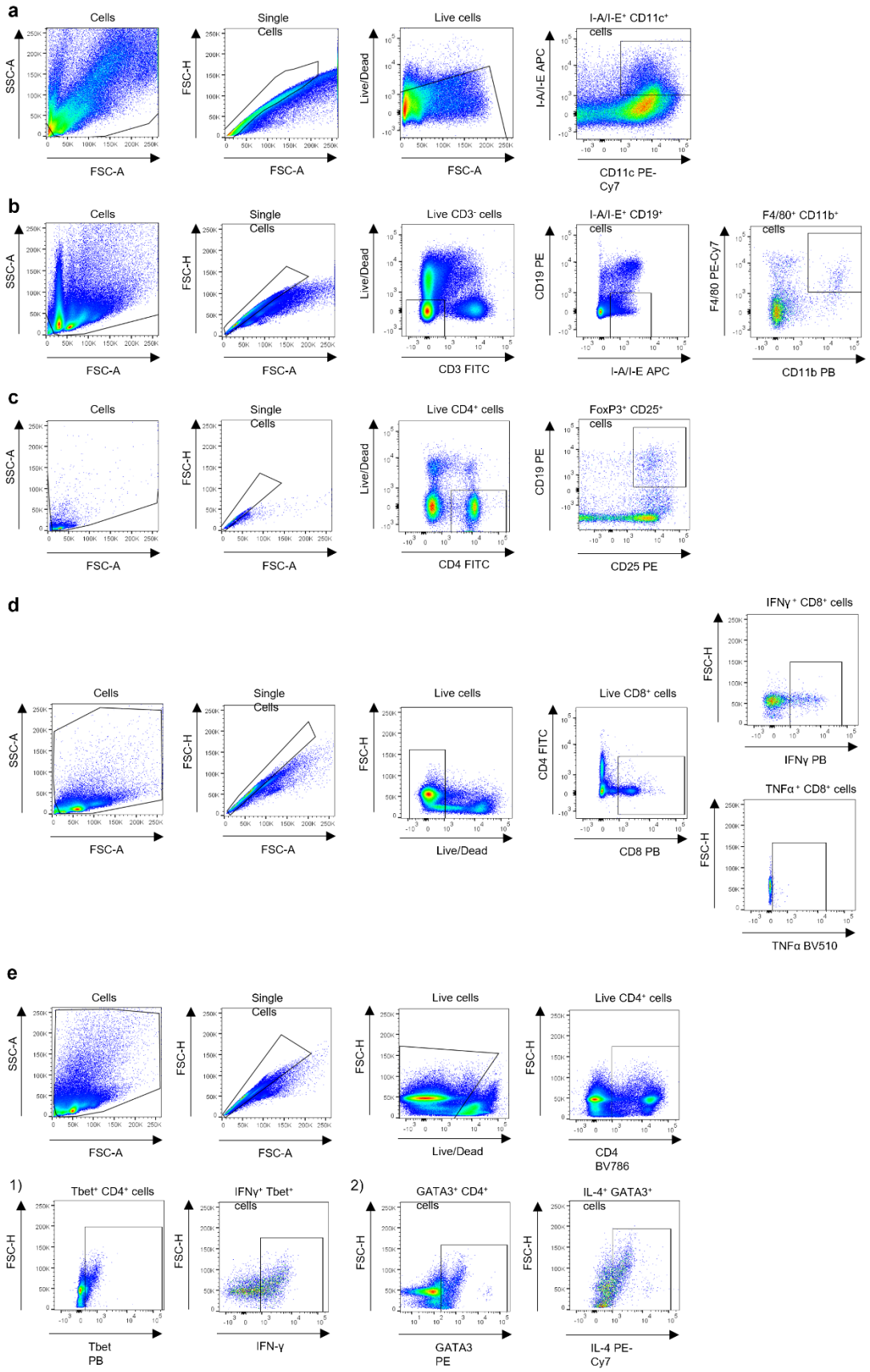
a
Cells
SSC-A
FSC-A
Single Cells
FSC-H
FSC-A
Live cells
Live/Dead
FSC-A
I-A/I-E⁺ CD11c⁺ cells
I-A/I-E APC
CD11c PE-Cy7
b
Cells
SSC-A
FSC-A
Single Cells
FSC-H
FSC-A
Live CD3⁻ cells
Live/Dead
CD3 FITC
I-A/I-E⁺ CD19⁺ cells
CD19 PE
I-A/I-E APC
F4/80⁺ CD11b⁺ cells
F4/80 PE-Cy7
CD11b PB
c
Cells
SSC-A
FSC-A
Single Cells
FSC-H
FSC-A
Live CD4⁺ cells
Live/Dead
CD4 FITC
FoxP3⁺ CD25⁺ cells
CD19 PE
CD25 PE
d
Cells
SSC-A
FSC-A
Single Cells
FSC-H
FSC-A
Live cells
FSC-H
Live/Dead
Live CD8⁺ cells
CD4 FITC
CD8 PB
IFNγ⁺ CD8⁺ cells
FSC-H
IFNγ PB
TNFα⁺ CD8⁺ cells
FSC-H
TNFα BV510
e
Cells
SSC-A
FSC-A
Single Cells
FSC-H
FSC-A
Live cells
FSC-H
Live/Dead
Live CD4⁺ cells
FSC-H
CD4 BV786
1)
Tbet⁺ CD4⁺ cells
FSC-H
Tbet PB
IFNγ⁺ Tbet⁺ cells
FSC-H
IFN-γ
2)
GATA3⁺ CD4⁺ cells
FSC-H
GATA3 PE
IL-4⁺ GATA3⁺ cells
FSC-H
IL-4 PE-Cy7

561

562 **Extended data figure 9. | a.** Representative gating strategy of dendritic cells. **b.** Representative gating
563 strategy of macrophages. **c.** Representative gating strategy of regulatory T cells. **d.** Representative gating
564 strategy of $CD8^+$ T cells. **e.** Representative gating strategy of T helper 1 (subpanel 1) and T helper 2 cells
565 (subpanel 2).

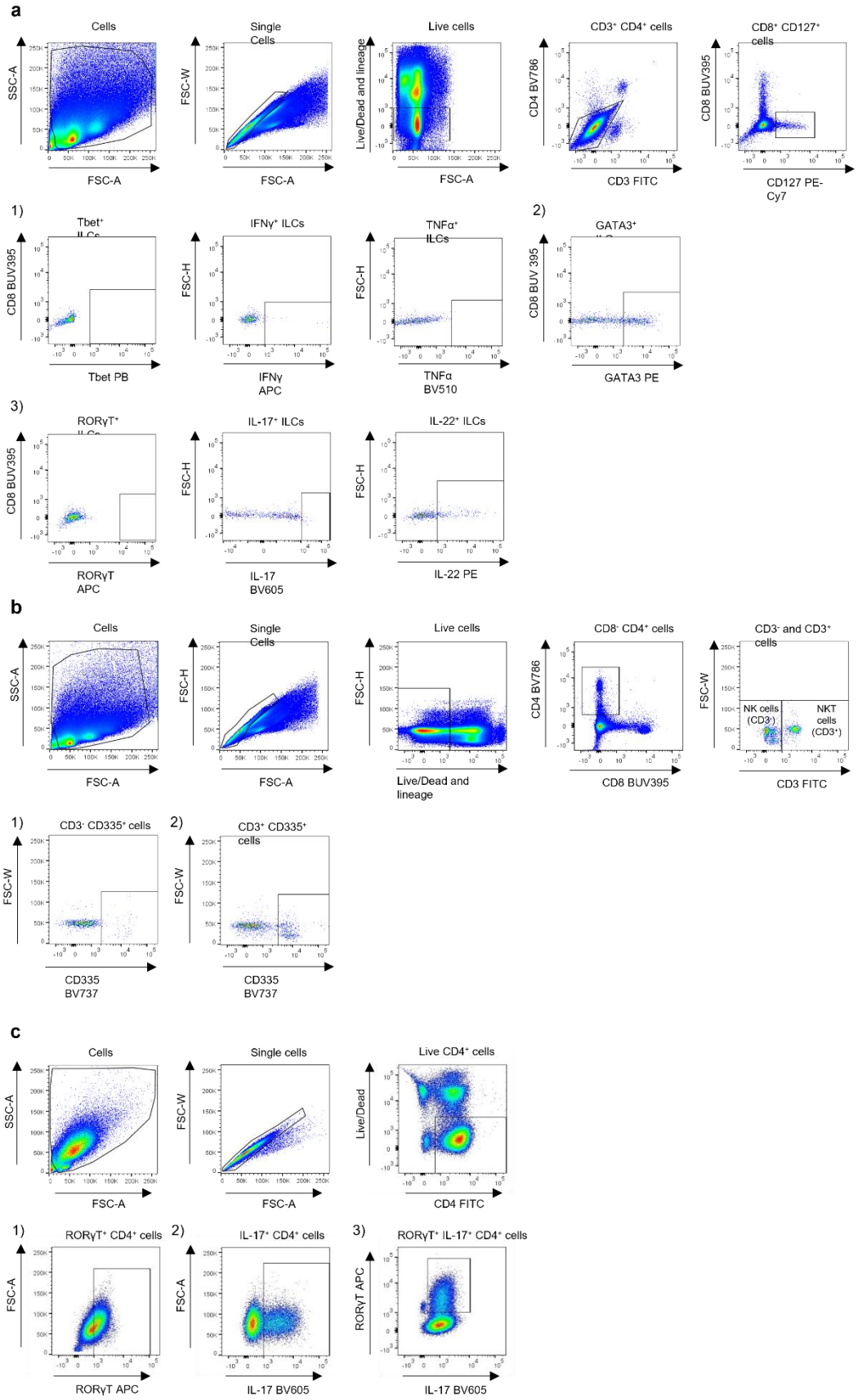
a
Cells
SSC-A
FSC-A
Single Cells
FSC-W
FSC-A
Live cells
Live/Dead and lineage
FSC-A
CD3+ CD4+ cells
CD4 BV786
CD3 FITC
CD8+ CD127+ cells
CD8 BUV395
CD127 PE-Cy7
1)
Tbet+ ILCs
CD8 BUV395
Tbet PB
IFNγ+ ILCs
FSC-H
IFNγ APC
TNFα+ ILCs
FSC-H
TNFα BV510
2)
GATA3+ ILCs
CD8 BUV 395
GATA3 PE
3)
RORγT+ ILCs
CD8 BUV395
RORγT APC
IL-17+ ILCs
FSC-H
IL-17 BV605
IL-22+ ILCs
FSC-H
IL-22 PE
b
Cells
SSC-A
FSC-A
Single Cells
FSC-H
FSC-A
Live cells
FSC-H
Live/Dead and lineage
CD8- CD4+ cells
CD4 BV786
CD8 BUV395
CD3- and CD3+ cells
FSC-W
NK cells (CD3-)
NKT cells (CD3+)
CD3 FITC
1)
CD3- CD335+ cells
FSC-W
CD335 BV737
2)
CD3+ CD335+ cells
FSC-W
CD335 BV737
c
Cells
SSC-A
FSC-A
Single cells
FSC-W
FSC-A
Live CD4+ cells
Live/Dead
CD4 FITC
1)
RORγT+ CD4+ cells
FSC-A
RORγT APC
2)
IL-17+ CD4+ cells
FSC-A
IL-17 BV605
3)
RORγT+ IL-17+ CD4+ cells
RORγT APC
IL-17 BV605

566

567 **Extended data figure 10. | a.** Representative gating strategy of innate lymphoid cells (ILC) - ILC1 (subpanel
568 1), ILC2 (subpanel 2), ILC3 (subpanel 3). Transcription factors and cytokines are stained in two separate
569 batches. **b.** Representative gating strategy of natural killer (subpanel 1) and natural killer T (subpanel 2)
570 cells. **c.** Representative gating strategy of T helper 17 cells – transcription-factor-based phenotyping
571 (subpanel 1), cytokine-based phenotyping (subpanel 2) and the combined strategy (subpanel 3).
572

573 **Acknowledgments**

574 We acknowledge the contributions of the following people in the context of this project and thank
575 them for their work: Dominik Ternes, Rubens Begaj, Martin Nurmik and Cedric Gilson (MDM group,
576 DLSM) for assistance during organ processing at experimental endpoint; Ysaline Bossicard (MDM group,
577 DLSM) for tissue cryosectioning; Stephanie Willieme, Eric Grant and Mahesh Desai (LIH) for processing of
578 murine fecal samples; Xiangyi Dong, Floriane Gavotto and Christian Jäger (LCSB Metabolomics Platform)
579 for metabolite profile acquisition and raw data analysis; Aurélien Ginolhac (DLSM) for contributions to
580 data pre-processing; Pau Perez Escriva (DLSM) for bacterial culturing and critical reading of the
581 manuscript; Giulia Cesi (DLSM) for her contributions to obtaining funding; Djalil Coowar, Jennifer Behm,
582 Julie Virolle, Cloe Ordrenneau and all other members of the Animal Facility Team (LCSB); Sara Gomez and
583 Eliane Klein (DLSM) for maintenance of organoid cultures and organoid experimentation; Rashi Halder for
584 fecal sample 16s and WGS sequencing. The sequencing experiments presented in this paper were carried
585 out at the LCSB sequencing platform (RRID: SCR_021931) at the University of Luxembourg. We also thank
586 the patients who contributed their samples to the national colorectal cancer cohort from which we
587 obtained the samples used in this study, as well as Christelle Bahlawane (CIEC), Eve Herkenne (CIEC),
588 Laetitia Garcia (CIEC), Ingrid Vreja (CIEC), and nurses from CIEC for contributing to this cohort. We thank
589 Dr. Barbara Kofler for her feedback and discussions during the course of the project. The experiments

presented in this paper were carried out using the high-performance computing facilities at the University of Luxembourg (https://hpc.uni.lu)[54]. BioRender (BioRender.com) was used for graphical illustration.

Funding

This work was supported by the Luxembourg National Research Fund (FNR) (grant nos. CORE/C16/BM/11282028 (E.L.), PoC/18/12554295 (E.L.), PRIDE17/11823097 (M.T.), PRIDE/11823097 (L.d.N.), and CORE/15/BM/10404093 (P.W.)), by the Luxembourg National Research Fund and the Fondation Cancer Luxembourg (grant no. CORE/C20/BM/14591557 (E.L.)) as well as by the Fondation du Pélican de Mie and Pierre Hippert-Faber under the aegis of the Fondation de Luxembourg ('Pelican Grant'; M.T. and M.M.), a FNRS-Télévie grant to M.M., no. 7.4565.21-40007364), an Internal Research Project at the University of Luxembourg (MiDiCa—integrated analysis of the effects of microbiome-diet interactions on human colorectal adenocarcinoma enterocytes; E.L., P.W. and S.H.), the Fondation Cancer and the Fondation Kriibskrank Kanner Luxembourg (V.I.P), the Action LIONS Vaincre le Cancer Luxembourg and a European Research Council grant under the European Union's Horizon 2020 research and innovation programme (grant agreement no. 863664 to P.W.). This project was also supported by the Doctoral School in Science and Engineering (M.T., M.K., M.M. and L.d.N.) and the Department of Life Sciences and Medicine at the University of Luxembourg. The funders had no role in study design, data collection and analysis, decision to publish or preparation of the manuscript.

612 **References**

613 1. Colorectal cancer statistics. *WCRF International* https://www.wcrf.org/cancer-trends/colorectal-
614 cancer-statistics/.
615 2. Akimoto, N. *et al.* Rising incidence of early-onset colorectal cancer - a call to action. *Nat. Rev. Clin.*
616 *Oncol.* **18**, 230–243 (2021).
617 3. Weber, D. D. *et al.* Ketogenic diet in the treatment of cancer – Where do we stand? *Mol. Metab.* **33**,
618 102–121 (2019).
619 4. Dmitrieva-Posocco, O. *et al.* β-Hydroxybutyrate suppresses colorectal cancer. *Nature* **605**, 160–165
620 (2022).
621 5. Ang, Q. Y. *et al.* Ketogenic Diets Alter the Gut Microbiome Resulting in Decreased Intestinal Th17
622 Cells. *Cell* **181**, 1263-1275.e16 (2020).
623 6. Kong, C. *et al.* Ketogenic diet alleviates colitis by reduction of colonic group 3 innate lymphoid cells
624 through altering gut microbiome. *Signal Transduct. Target. Ther.* **6**, 154 (2021).
625 7. Wei, R. *et al.* Ketogenesis Attenuates KLF5-Dependent Production of CXCL12 to Overcome the
626 Immunosuppressive Tumor Microenvironment in Colorectal Cancer. *Cancer Res.* **82**, 1575–1588
627 (2022).
628 8. Ferrere, G. *et al.* Ketogenic diet and ketone bodies enhance the anticancer effects of PD-1 blockade.
629 *JCI Insight* **6**, 145207 (2021).
630 9. Paoli, A. *et al.* Ketogenic Diet and Microbiota: Friends or Enemies? *Genes* **10**, 534 (2019).
631 10. Cairo, C. & Webb, T. J. Effective Barriers: The Role of NKT Cells and Innate Lymphoid Cells in the Gut.
632 *J. Immunol. Baltim. Md 1950* **208**, 235–246 (2022).
633 11. Jukic, A., Bakiri, L., Wagner, E. F., Tilg, H. & Adolph, T. E. Calprotectin: from biomarker to biological
634 function. *Gut* **70**, 1978–1988 (2021).

635 12. Wong, S. H. *et al.* Gavage of Fecal Samples From Patients With Colorectal Cancer Promotes
636 Intestinal Carcinogenesis in Germ-Free and Conventional Mice. *Gastroenterology* **153**, 1621-1633.e6
637 (2017).
638 13. Mu, C. *et al.* Probiotics counteract hepatic steatosis caused by ketogenic diet and upregulate AMPK
639 signaling in a model of infantile epilepsy. *EBioMedicine* **76**, 103838 (2022).
640 14. Nan, F. *et al.* Mannose: A Sweet Option in the Treatment of Cancer and Inflammation. *Front.*
641 *Pharmacol.* **13**, (2022).
642 15. Gonzalez, P. S. *et al.* Mannose impairs tumour growth and enhances chemotherapy. *Nature* **563**,
643 719–723 (2018).
644 16. Liu, Q., Li, X., Zhang, H. & Li, H. Mannose Attenuates Colitis-Associated Colorectal Tumorigenesis by
645 Targeting Tumor-Associated Macrophages. *J. Cancer Prev.* **27**, 31–41 (2022).
646 17. De Simone, V., Pallone, F., Monteleone, G. & Stolfi, C. Role of TH17 cytokines in the control of
647 colorectal cancer. *Oncoimmunology* **2**, e26617 (2013).
648 18. Ternes, D. *et al.* Microbiome in Colorectal Cancer: How to Get from Meta-omics to Mechanism?
649 *Trends Microbiol.* **28**, 401–423 (2020).
650 19. Fan, L. *et al.* A. Muciniphila Suppresses Colorectal Tumorigenesis by Inducing TLR2/NLRP3-Mediated
651 M1-Like TAMs. *Cancer Immunol. Res.* **9**, 1111–1124 (2021).
652 20. Wardman, J. F., Bains, R. K., Rahfeld, P. & Withers, S. G. Carbohydrate-active enzymes (CAZymes) in
653 the gut microbiome. *Nat. Rev. Microbiol.* **20**, 542–556 (2022).
654 21. Han, S. *et al.* A metabolomics pipeline for mechanistic interrogation of the gut microbiome. *Nature*
655 **595**, 415–420 (2021).
656 22. Mao, T. *et al.* Elevated serum β-hydroxybutyrate, a circulating ketone metabolite, accelerates
657 colorectal cancer proliferation and metastasis via ACAT1. *Oncogene* **42**, 1889–1899 (2023).

658 23. Gopalakrishnan, V. *et al.* Gut microbiome modulates response to anti-PD-1 immunotherapy in
659 melanoma patients. *Science* **359**, 97–103 (2018).
660 24. Matson, V. *et al.* The commensal microbiome is associated with anti-PD-1 efficacy in metastatic
661 melanoma patients. *Science* **359**, 104–108 (2018).
662 25. Routy, B. *et al.* Gut microbiome influences efficacy of PD-1-based immunotherapy against epithelial
663 tumors. *Science* **359**, 91–97 (2018).
664 26. Olson, C. A. *et al.* The Gut Microbiota Mediates the Anti-Seizure Effects of the Ketogenic Diet. *Cell*
665 **173**, 1728-1741.e13 (2018).
666 27. cis-Encoded Small RNAs, a Conserved Mechanism for Repression of Polysaccharide Utilization in
667 Bacteroides | Journal of Bacteriology. https://journals.asm.org/doi/10.1128/jb.00381-16.
668 28. Pudlo, N. A. *et al.* Symbiotic Human Gut Bacteria with Variable Metabolic Priorities for Host Mucosal
669 Glycans. *mBio* **6**, 10.1128/mbio.01282-15 (2015).
670 29. Milani, C. *et al.* Bifidobacteria exhibit social behavior through carbohydrate resource sharing in the
671 gut. *Sci. Rep.* **5**, 15782 (2015).
672 30. Luis, A. S. & Hansson, G. C. Intestinal mucus and their glycans: A habitat for thriving microbiota. *Cell*
673 *Host Microbe* **31**, 1087–1100 (2023).
674 31. Drula, E. *et al.* The carbohydrate-active enzyme database: functions and literature. *Nucleic Acids*
675 *Res.* **50**, D571–D577 (2022).
676 32. Desai, M. S. *et al.* A dietary fiber-deprived gut microbiota degrades the colonic mucus barrier and
677 enhances pathogen susceptibility. *Cell* **167**, 1339-1353.e21 (2016).
678 33. van der Lugt, B. *et al.* Akkermansia muciniphila ameliorates the age-related decline in colonic mucus
679 thickness and attenuates immune activation in accelerated aging Ercc1−/Δ7 mice. *Immun. Ageing*
680 **16**, 6 (2019).

681 34. Gamage, H. K. A. H. *et al.* Changes in dietary fiber intake in mice reveal associations between colonic
682 mucin O-glycosylation and specific gut bacteria. *Gut Microbes* **12**, 1802209 (2020).
683 35. Johansson, M. E. V. *et al.* Normalization of Host Intestinal Mucus Layers Requires Long-Term
684 Microbial Colonization. *Cell Host Microbe* **18**, 582–592 (2015).
685 36. Brown, E. M., Clardy, J. & Xavier, R. J. Gut microbiome lipid metabolism and its impact on host
686 physiology. *Cell Host Microbe* **31**, 173–186 (2023).
687 37. Yamada, S. *et al.* Gut microbiota-mediated generation of saturated fatty acids elicits inflammation in
688 the liver in murine high-fat diet-induced steatohepatitis. *BMC Gastroenterol.* **17**, 136 (2017).
689 38. Guillou, H., Zadravec, D., Martin, P. G. P. & Jacobsson, A. The key roles of elongases and desaturases
690 in mammalian fatty acid metabolism: Insights from transgenic mice. *Prog. Lipid Res.* **49**, 186–199
691 (2010).
692 39. Yao, J. & Rock, C. O. Exogenous fatty acid metabolism in bacteria. *Biochimie* **141**, 30–39 (2017).
693 40. Flowers, M. T. & Ntambi, J. M. Role of stearoyl-coenzyme A desaturase in regulating lipid
694 metabolism. *Curr. Opin. Lipidol.* **19**, 248–256 (2008).
695 41. Lien, E. C. *et al.* Low glycaemic diets alter lipid metabolism to influence tumour growth. *Nature* **599**,
696 302–307 (2021).
697 42. Zhou, X. *et al.* Stearoyl-CoA Desaturase-Mediated Monounsaturated Fatty Acid Availability Supports
698 Humoral Immunity. *Cell Rep.* **34**, (2021).
699 43. Grajchen, E. *et al.* Fatty acid desaturation by stearoyl-CoA desaturase-1 controls regulatory T cell
700 differentiation and autoimmunity. *Cell. Mol. Immunol.* **20**, 666–679 (2023).
701 44. Kindt, A. *et al.* The gut microbiota promotes hepatic fatty acid desaturation and elongation in mice.
702 *Nat. Commun.* **9**, 3760 (2018).
703 45. Kim, K. S. *et al.* Genome-wide multi-omics analysis reveals the nutrient-dependent metabolic
704 features of mucin-degrading gut bacteria. *Gut Microbes* **15**, 2221811 (2023).

705 46. McKain, N., Shingfield, K. J. & Wallace, R. J. Metabolism of conjugated linoleic acids and 18 : 1 fatty
706 acids by ruminal bacteria: products and mechanisms. *Microbiology* **156**, 579–588 (2010).
707 47. Microbial Production of Conjugated Linoleic Acid and Conjugated Linolenic Acid Relies on a
708 Multienzymatic System | Microbiology and Molecular Biology Reviews.
709 https://journals.asm.org/doi/10.1128/mmbr.00019-18.
710 48. Fermor, B. F. *et al.* Fatty acid composition of normal and malignant cells and cytotoxicity of stearic,
711 oleic and sterculic acids in vitro. *Eur. J. Cancer Oxf. Engl. 1990* **28A**, 1143–1147 (1992).
712 49. Habib, N. A. *et al.* Stearic acid and carcinogenesis. *Br. J. Cancer* **56**, 455–458 (1987).
713 50. Evans, L. M., Cowey, S. L., Siegal, G. P. & Hardy, R. W. Stearate preferentially induces apoptosis in
714 human breast cancer cells. *Nutr. Cancer* **61**, 746–753 (2009).
715 51. Mitchel, J. *et al.* Computational Identification of Stearic Acid as a Potential PDK1 Inhibitor and In
716 Vitro Validation of Stearic Acid as Colon Cancer Therapeutic in Combination with 5-Fluorouracil.
717 *Cancer Inform.* **20**, 11769351211065979 (2021).
718 52. Zhang, Y. *et al.* Altered gut microbiome composition in children with refractory epilepsy after
719 ketogenic diet. *Epilepsy Res.* **145**, 163–168 (2018).
720 53. Naqash, A. R. *et al.* The role of gut microbiome in modulating response to immune checkpoint
721 inhibitor therapy in cancer. *Ann. Transl. Med.* **9**, 1034 (2021).
722 54. Varrette, S., Bouvry, P., Cartiaux, H. & Georgatos, F. Management of an academic HPC cluster: The
723 UL experience. in *2014 International Conference on High Performance Computing & Simulation*
724 *(HPCS)* 959–967 (IEEE, 2014). doi:10.1109/HPCSim.2014.6903792.
725